Review

Titanium Lattice Structures Produced via Additive Manufacturing for a Bone Scaffold: A Review

Fabio Distefano [1], Salvatore Pasta [2,3],* and Gabriella Epasto [1]

[1] Department of Engineering, University of Messina, C.da Di Dio, 98166 Messina, Italy
[2] Department of Engineering, University of Palermo, Viale delle Scienze, 90128 Palermo, Italy
[3] Department of Research, IRCCS ISMETT, Via Tricomi n.5, 90127 Palermo, Italy
*   Correspondence: salvatore.pasta@unipa.it

Abstract: The progress in additive manufacturing has remarkably increased the application of lattice materials in the biomedical field for the fabrication of scaffolds used as bone substitutes. Ti6Al4V alloy is widely adopted for bone implant application as it combines both biological and mechanical properties. Recent breakthroughs in biomaterials and tissue engineering have allowed the regeneration of massive bone defects, which require external intervention to be bridged. However, the repair of such critical bone defects remains a challenge. The present review collected the most significant findings in the literature of the last ten years on Ti6Al4V porous scaffolds to provide a comprehensive summary of the mechanical and morphological requirements for the osteointegration process. Particular attention was given on the effects of pore size, surface roughness and the elastic modulus on bone scaffold performances. The application of the Gibson–Ashby model allowed for a comparison of the mechanical performance of the lattice materials with that of human bone. This allows for an evaluation of the suitability of different lattice materials for biomedical applications.

Keywords: lattice structures; titanium alloy; bone tissue engineering; scaffolds; additive manufacturing; mechanical properties

1. Introduction

Lattice structures are topologically ordered structures based on one or more repeating unit cells [1]. From Gibson–Ashby's research on cellular solids, a unit cell is determined by the connectivity and dimensions of its constitutive strut elements, which are connected at specific nodes [2]. Lattice materials present voids deliberately embedded in their structures [2]. Three types of lattice structures are currently studied for engineering applications: strut-based, triply periodic minimal surfaces (TPMS) skeletal and TPMS sheet [3].

In recent years, the application of lattice structures in engineering fields has considerably grown due to the progress in Additive Manufacturing (AM). Freedom of design, mass customization, waste minimization, the ability to manufacture complex structures and rapid prototyping are the major advantages of AM [4]. The ability to fabricate components with complex parts and customizable material properties is one of the most important advantages of these technologies, allowing for the production of complex functional objects from multiple materials unattainable with conventional manufacturing methods [5]. The modern approaches to fabricate bone constructs via AM provide a favourable environment for bone regeneration [6]. Different AM technologies are currently used for the fabrication of parts from metallic fine powders, for instance: Selective Laser Melting (SLM) [7], Selective Laser Sintering (SLS) [8], Direct Metal Laser Sintering (DMLS) [9], Electron Beam Melting (EBM) [10].

Lattice materials attract a great deal of interest in several engineering disciplines, for instance automotive and aerospace, thanks to the high strength-to-weight ratio, thermal conductivity and enhanced mechanical energy absorption [11,12]. Applications in the biomechanical field used as bone substitutes have been also proposed [13–16].

The Ti6Al4V alloy has a long history of application for bone implants due to its mechanical biocompatibility, high strength, long lifetime, high wear resistance and low elastic modulus [17–19].

The mechanical and morphological features of lattice materials affect the osteointegration and bone ingrowth of the candidate implant. Specifically, the elastic modulus was demonstrated to affect scaffold remodelling [20], as well as cell migration and differentiation [21]. It is particularly important to reduce or eliminate stress shielding, which is one of the primary causes requiring revision surgery leading to bone resorption [22,23]. Other important factors are pore size, which affects cell penetration and bone ingrowth [24,25], and surface roughness, which supports the achievement of improved interaction mechanisms between the implant and biological tissues [26,27].

This review aims to provide a comprehensive view of the mechanical and morphological requirements of lattice structures for the design of biomedical implants for bone substitutes, with a focus on the effect of pore size and surface roughness on the bone ingrowth and on the effect of the elastic modulus in the reduction of stress shielding and promotion of osseointegration. The current work intends to furnish guidelines on the choice of the most suitable lattice topology by applying the Gibson–Ashby model and by focusing on the performance and features needed for bone stimulation in the osseointegration process. The review has collected the most significant findings achieved in the last ten years with the utilization of additive manufacturing with Ti6Al4V for porous scaffolds.

2. Classification of Lattice Structures

Three classes of lattice structures are commonly investigated in applications for biomedical engineering: the first class is strut-based structures, while the second and third classes are derived from mathematically-created TPMS, namely skeletal-TPMS and sheet-TPMS lattice structures.

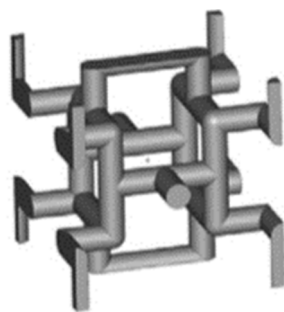Figure 1 shows the strut-based unit cell [2,28] proposed by Gibson–Ashby.

Figure 1. Gibson–Ashby lattice structure [3].

The most known strut-based topologies, which are named after analogous crystalline structures, are the body centred cubic (BCC) and face centred-cubic (FCC), as well as the variations named z-struts BCCZ and FCCZ. There exist other strut-based topologies, such as the cubic, octet-truss and diamond (see Figure 2).
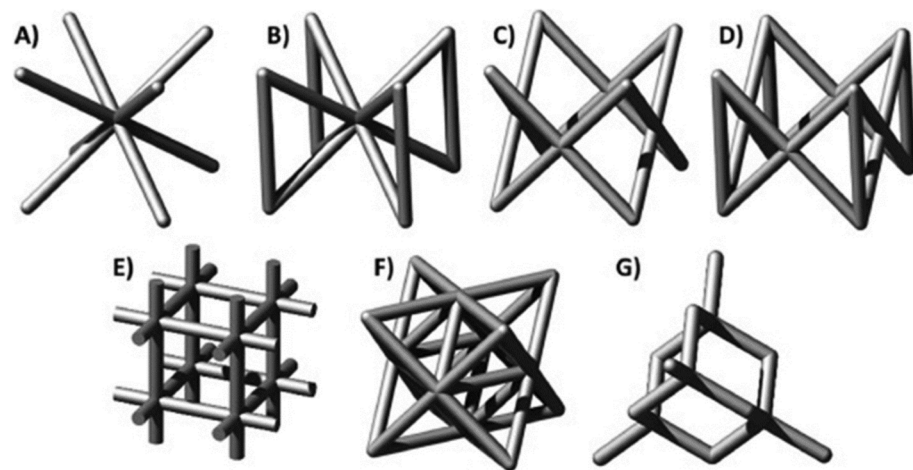
Figure 2. Strut-based lattice topologies: (**A**) BCC; (**B**) BCCZ; (**C**) FCC; (**D**) FCCZ; (**E**) cubic; (**F**) octet-truss; (**G**) diamond [29].

The octet-truss cell is composed of an octahedral cell (black part) and a tetrahedral cell (light grey part), as shown in Figure 3.
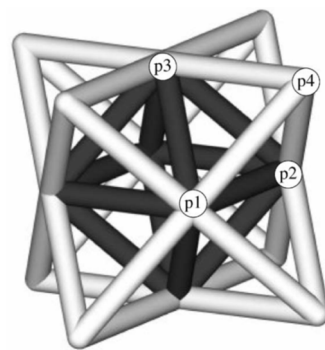

Figure 3. Structure of the octet-truss unit cell [30].

Other variations in the BCC lattice are represented by the G7 unit cell and the simple cubic body-centred cubic (SCBCC) as shown in Figure 4.
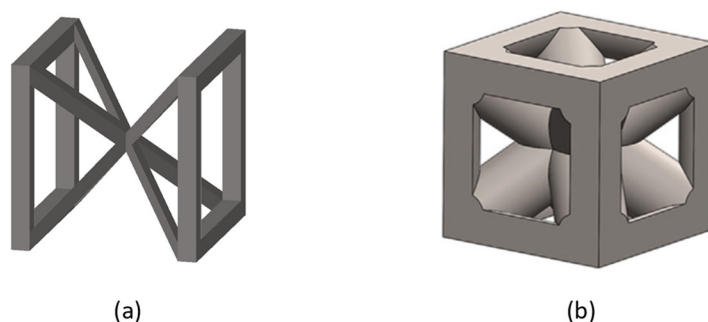

(a) (b)

Figure 4. BCC-derived lattice structures: (**a**) G7; (**b**) SCBCC [31].

Lattice materials with cubic symmetry, strut-based cell topology, such as Archimedean solids or Catalan solids, have been widely investigated over the years. Archimedean solids are a group of 13 solids, first enumerated by Archimedes (see Figure 5). They are convex uniform polyhedra composed of regular polygons with identical vertices. Catalan solids are the dual polyhedra of the Archimedean solids. Most studied Archimedean solids include the cuboctahedron [32,33], truncated cube (TC) [34,35], truncated octahedron (TO or Kelvin cell) [36,37], rhombicuboctahedron (RCO) [35,38] and truncated cuboctahedron

(TCO) [35,39]. Among Catalan solids, researchers mostly focused their attention on the rhombic dodecahedron (RD) [35,40].
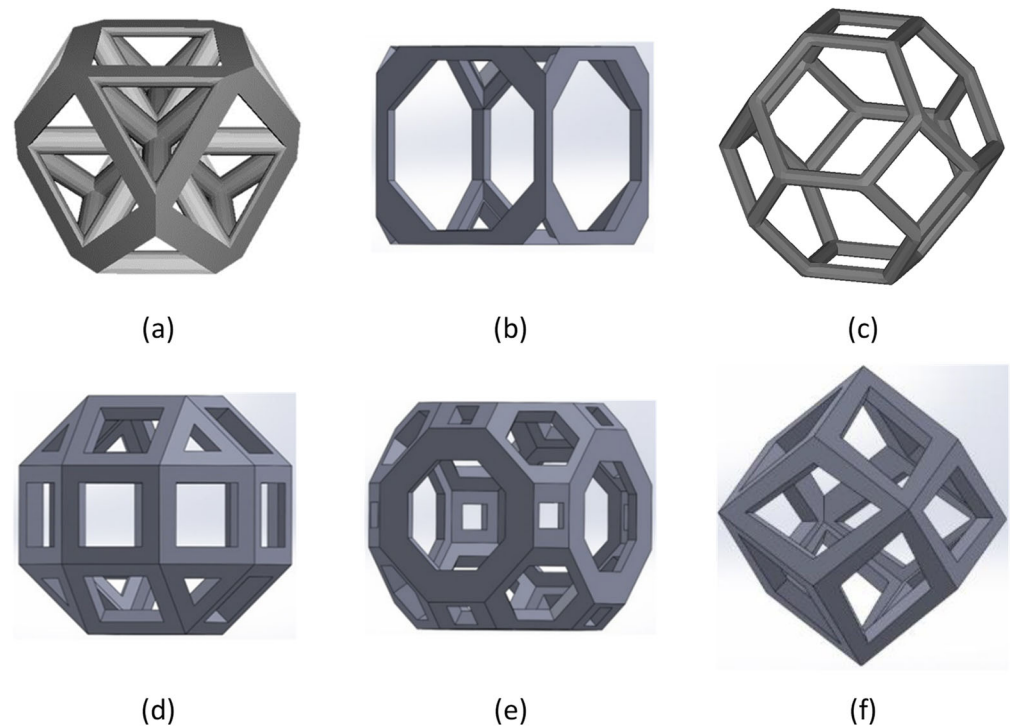

Figure 5. Archimedean and Catalan solid lattice structures: (**a**) cuboctahedron; (**b**) truncated cube; (**c**) truncated octahedron (Kelvin); (**d**) rhombicuboctahedron; (**e**) truncated cuboctahedron; (**f**) rhombic dodecahedron [33,35].

Recently, cellular structures with mathematically defined architectures, as TPMS based topologies, have been proposed [3]. A minimal surface can be considered as a surface with a mean curvature equal to zero in all points; thus, a TPMS is characterized as a minimal surface periodic in three independent directions [41]. TPMS mathematical representation is defined by a system of coordinates calculated using the Enneper–Weierstrass parametric representation as shown here.

$$\begin{cases} x = \mathrm{Re}\left(e^{i\theta} \int_{w_0}^{w} \left(1 - \tau^2\right) R(\tau) d\tau\right) \\ y = \mathrm{Re}\left(e^{i\theta} \int_{w_0}^{w} i\left(1 - \tau^2\right) R(\tau) d\tau\right) \\ z = \mathrm{Re}\left(e^{i\theta} \int_{w_0}^{w} 2\tau R(\tau) d\tau\right) \end{cases} \tag{1}$$

$R(\tau)$ represents a function dependent upon the TPMS topology and can be expressed as:
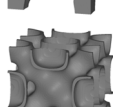
$$R(t) = \frac{1}{\sqrt{1 - 14\tau^4 + \tau^8}} \tag{2}$$

Compared to the parametric form, a TPMS has a simpler and unified representation expressed by sinusoid terms and defined as [41]:

$$\varphi(\gamma) = \sum_{k=1}^{K} A_k \cos\left[\frac{2\pi(h_k \cdot \gamma)}{\lambda_k} + p_k\right] = C \tag{3}$$

TPMS topologies can be approximately defined as combinations of trigonometric functions in an implicit form. Examples of the most common TPMS equations in the implicit form are expressed in Table 1 as follows [42,43]:

Table 1. Examples of the most common TPMS equations.

	$\varphi_{\text{primitive}} \equiv \cos x + \cos y + \cos z = C$
	$\varphi_{\text{gyroid}} \equiv \sin x \cos y + \sin z \cos x + \sin y \cos z = C$
	$\varphi_{\text{diamond}} \equiv \cos x \cos y \cos z - \sin x \sin y \sin z = C$
	$\varphi_{\text{IWP}} \equiv 2(\cos x \cos y + \cos y \cos z + \cos z \cos x) - (\cos 2x + \cos 2y + \cos 2z) = C$
	$\varphi_{\text{FRD}} \equiv 4(\cos x \cos y \cos z) - (\cos 2x \cos 2y + \cos 2y \cos 2z + \cos 2z \cos 2x) = C$
	$\varphi_{\text{Neovius}} \equiv 3(\cos x + \cos y + \cos z) + 4 \cos x \cos y \cos z = C$

Two classes of TPMS lattices can be considered, namely sheet TPMS and skeletal TPMS. Some TPMS lattices were investigated in both versions, such as gyroid [44,45], diamond [15,46] and IWP [47,48]. Other TPMS structures have been studied only in the sheet-based version: Schwarz primitive [49,50], FRD [47,51] and Neovius [52,53]. Figure 6 shows commonly known TPMS structures.

(a)   (b)   (c)
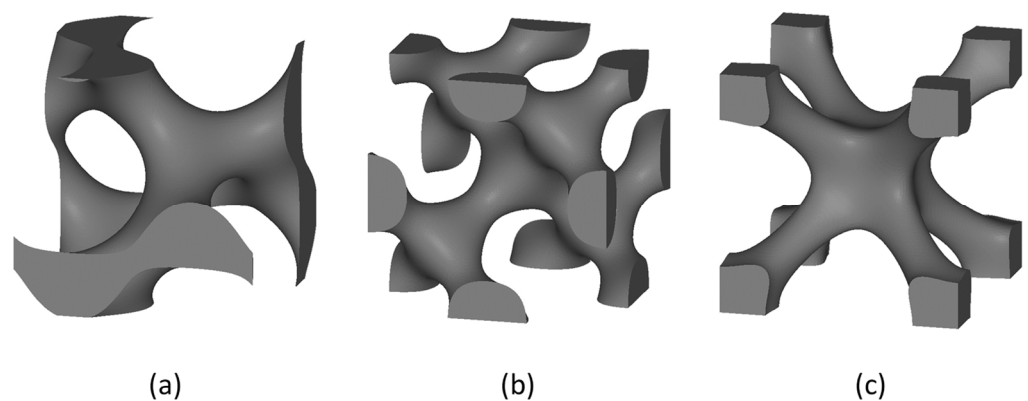
Figure 6. *Cont.*

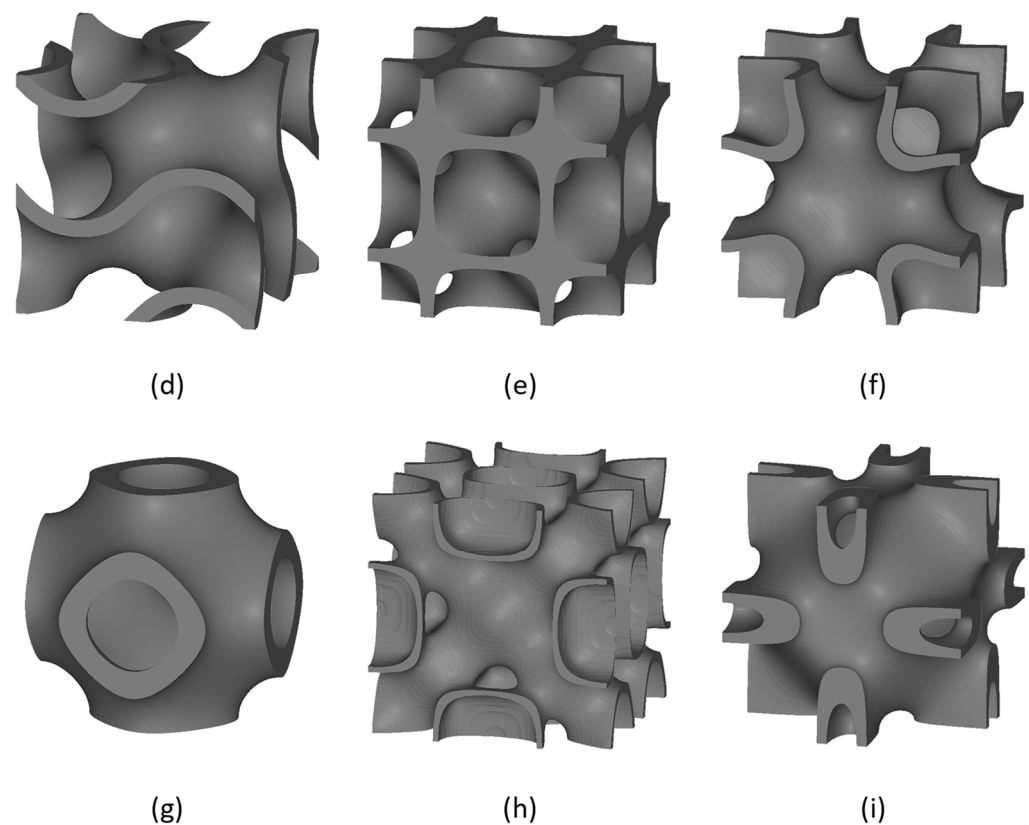**Figure 6.** TPMS lattice structures: (**a**) skeletal gyroid; (**b**) skeletal diamond; (**c**) skeletal IWP; (**d**) sheet gyroid; (**e**) sheet diamond; (**f**) sheet IWP; (**g**) Schwarz primitive; (**h**) FRD; (**i**) Neovius.

Over the last few years, novel lattice materials have been proposed (see Figure 7). Dong et al. [54] numerically and experimentally investigated the mechanical behaviour of a vintile single unit cell and lattice, while other researchers analysed its behaviour for biomedical applications [55,56]. Alomar et al. [57] proposed and developed a new lattice material based on a circular constituent cell. Distefano et al. [58] developed a novel biomimetic lattice material based on the scheme of rocks and called the TAOR lattice.
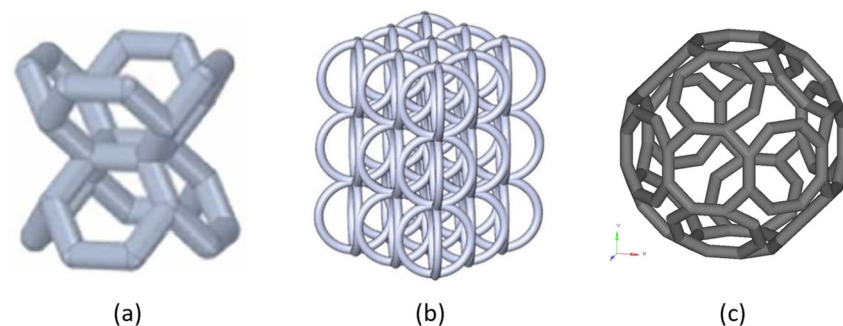
Figure 7. Novel designed lattice materials: (**a**) vintile cell; (**b**) circular cell-based lattice; (**c**) TAOR cell [57–59].

3. Current Status of Additive Manufacturing Technologies

AM has grown considerably in recent years, thanks to the technological advancement and the subsequent enhanced material properties. The ability to create components with complex parts and customisable material properties is one of the most important advantages of AM, allowing the fabrication of complex functional objects from various materials unattainable with conventional manufacturing methods [5]. This resulted in the industrial use of AM parts, even in highly advanced applications, most notably in

aerospace, automotive and biomedical fields. Different AM technologies are currently used for the fabrication of parts used in this fields, from metallic fine powders, for instance: SLM, DMLS, EBM [10].

However, due to the rapid diffusion of a multitude of technologies related to AM, there is a lack of a comprehensive set of design principles, manufacturing guidelines and standardization of best practices. AM techniques require process optimization and quality control to ensure accuracy and reliability [60]. This requirement is particularly relevant for components with complex geometries, such as lattice structures, which include curved surfaces and thin connecting features. Different factors, such as machine selection, processes and materials, position and orientation of the part and finishing can alter the resulting quality of the printed component [61]. A major limitation is the minimum feature size for the AM technology used [62], the achievable feature resolution is inherently constrained by the fact that powder-based technologies require particles larger than 20 μm so that the powder can be successfully spread during recoating [63]. An additional limitation is placed on the part design, most notably the build angles [64]. When extremely complex structure, such as truncated icosahedra, are printed with dimensions in the order of micrometres, some feature cannot be reproduced [65]. An important attribute is the surface quality, which is mainly determined by the thickness of each printed layer. Surface quality also depends on the form of the raw material; powder bed AM processes present poorer surface quality than others due to large and partially melted powder particles that reside on the printed part's surface [61].

In order to promote research interest and investments, the goal of AM technologies is to face these and other challenges to ensure the quality of the 3D-printed products [66].

4. Mechanical and Morphological Requirements for Biomedical Applications

Bone is a complex tissue undergoing biological remodelling. This feature of bone underpins the ability to remodel itself to repair damage [67]. However, the bone's ability for self-regeneration of massive defects can be limited because of deficiencies in blood supply or in the presence of systemic disease [68]. When bone defects exceed a critical non-healable size, a surgical process is required to support self-healing when defects need bridging. Despite recent advances in biomaterials and tissue engineering, the repair of such a critical bone defects remains a challenge [69–71]. Lattice materials are widely used in the biomedical field when devices are applied as bone substitutes [72–79]. A successful porous metallic implant should restore the physiological function of the bone, and porous structures provide high interfacial bond area for vascularization and bone ingrowth, promoting the biological fixation of implants and bone [80]. An ideal bone porous implant should possess the following properties: biocompatibility, suitable surface for cell attachment, proliferation, differentiation and migration [67]. In addition, angiogenesis is an essential physiological process for bone regeneration [81]; the biological inertia of the Ti6Al4V surface and the deficit of angiogenesis may cause postoperative complications, such as dislocation or loosening of the device [82]. Several methods to enhance the angiogenesis of Ti6Al4V scaffolds were evaluated in the literature, including the development of multifunctional surface coatings with angiogenic properties [83]; the incorporation into a Ti6Al4V alloy of copper ions, which presents high bioactivity and outstanding antibacterial properties [84]; and the controlled release of bone-morphogenic protein-2 and vascular endothelial growth factor in the Ti6Al4V alloy [85]. The abilities of bone-lining cells are affected by the size and shape of the scaffold pores; higher porosity promotes cell ingrowth and the transport of nutrients [86]. The current review presents a comparison of literature findings to evaluate the effect of mechanical and morphological properties on bone ingrowth and osseointegration and estimate the optimal parameters of lattice structures for biomedical applications.

4.1. Effect of Pore Size

The influence of pore size is still controversial. Wang et al. [67] reported that the optimal pore size is in the range of 100–400 μm. However, several studies evaluated the

influence of pore size on bone ingrowth, with controversial results. Van Bael et al. [87] produced, via SLM, six Ti6Al4V scaffold configurations with three different pore shapes (triangular, hexagonal and rectangular) and two distinct pore sizes (500 μm and 1000 μm); after 14 days, in vitro culture exhibited a significantly higher living cell density on the Ti6Al4V bone scaffolds with 1000 μm pores. Cheng et al. [88] used a human trabecular bone template to design and manufacture Ti6Al4V scaffolds with variable porosities via SLS and observed increasing bone ingrowth up to 300 μm. The latter was considered an optimal value for bone ingrowth. Prananingrum et al. [89] fabricated porous titanium scaffolds stratified in four groups with increasing pore sizes from 60 μm up to 600 μm. After 20 weeks, the group with a pore size of 100 μm showed considerably greater bone ingrowth compared to the other groups. Li et al. [90] fabricated Ti6Al4V scaffolds with three pore sizes between 300 μm and 700 μm using Electron Beam Melting (EBM). Bone ingrowth in the group with a pore size of 400 μm was significantly higher than that with the other two porous scaffolds. Taniguchi et al. [91] implanted 300 μm, 600 μm and 900 μm porous titanium scaffolds into rabbit tibia and found that 600 μm and 900 μm scaffolds demonstrated significantly higher bone ingrowth than 300 μm scaffolds. Kapat et al. [92] used Ti6Al4V samples with 92 μm, 178 μm and 297 μm pore sizes; a quantitative evaluation of bone ingrowth via μ-CT revealed that there was approximately 52% higher bone formation in the sample with a 178 μm pore size after 12 weeks, compared to that with the other configurations. Ran et al. [93] designed and fabricated porous Ti6Al4V implants with straightforward pore dimensions: 500, 700, and 900 μm using SLM. They assessed the morphological features of scaffolds, showing that actual pore sizes were about 400, 600 and 800 μm; they observed that the biological performance of specimens with a 600 μm pore size was superior to that of the other two groups. Luan et al. [94] examined porous Ti6Al4V scaffolds with 334.1 μm, 383 μm and 401 μm pore sizes; results highlighted that all three types of porous Ti6Al4V scaffolds were inclined to promote bone ingrowth; however, a pore size of 383 μm showed better results. Ouyang et al. [95] fabricated, via SLM, porous titanium scaffolds with similar porosity and different pore sizes: 400, 650, 850 and 1100 μm; the best bone ingrowth was observed in scaffold with a 650 μm pore size. Chen et al. [96] manufactured, via SLM, scaffolds with 500 μm, 600 μm and 700 μm pore sizes and 60% and 70% porosities to explore the optimal morphological features. The scaffold with a pore size of 500 μm and porosity of 60% exhibited the best bone ingrowth by means of in vivo experiments. Wang et al. fabricated, via EBM, seven groups of porous scaffolds with pore sizes from 800 μm to 1000 μm. Bone ingrowth was assessed via μ-CT 3D reconstruction images showed the magnitude of positive remodelling with 1000 μm-pore-size scaffolds. Table 2 and Figure 8 describe the aforementioned findings in chronological order.

Table 2. Comparison of different research findings for the evaluation of the optimal pore size for bone ingrowth.

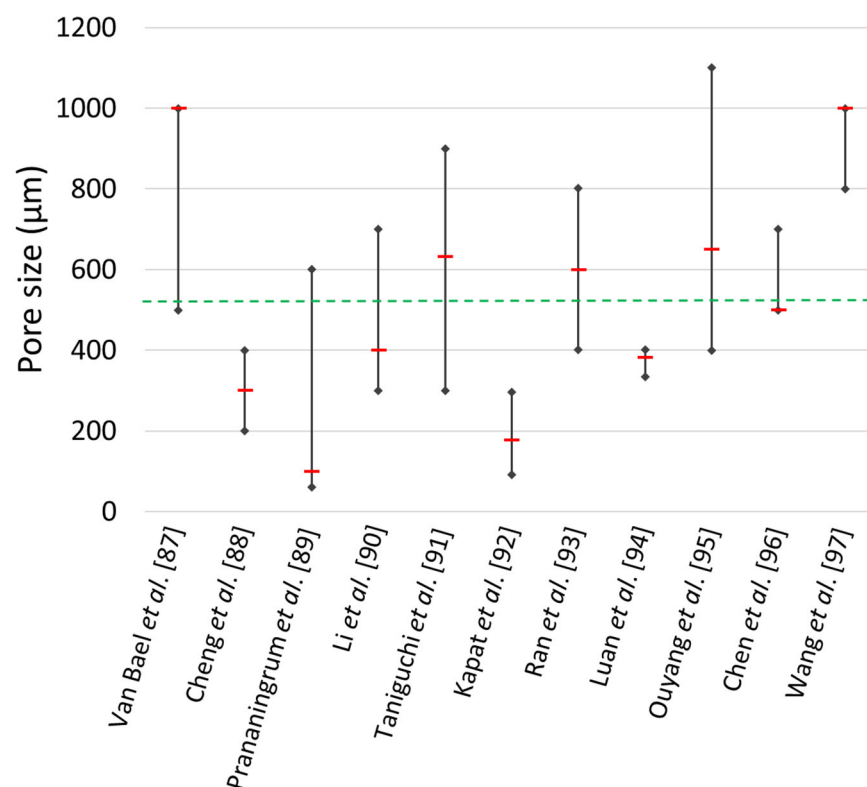| Research	Optimal Pore Size [μm]	Tested Pore Size Range [μm]
Van Bael et al. [87]	1000	500–1000
Cheng et al. [88]	300	200–400
Prananingrum et al. [89]	100	60–600
Li et al. [90]	400	300–700
Taniguchi et al. [91]	632	300–900
Kapat et al. [92]	178	92–297
Ran et al. [93]	600	400–800
Luan et al. [94]	383	334–401
Ouyang et al. [95]	650	400–1100
Chen et al. [96]	500	500–700
Wang et al. [97]	1000	800–1000

Figure 8. Evaluated optimal pore size for bone ingrowth.

All presented results were obtained by performing in vivo or in vitro experiments where μ-CT reconstructions were applied to quantitatively show the effect of pore size on bone ingrowth (see Figure 9).
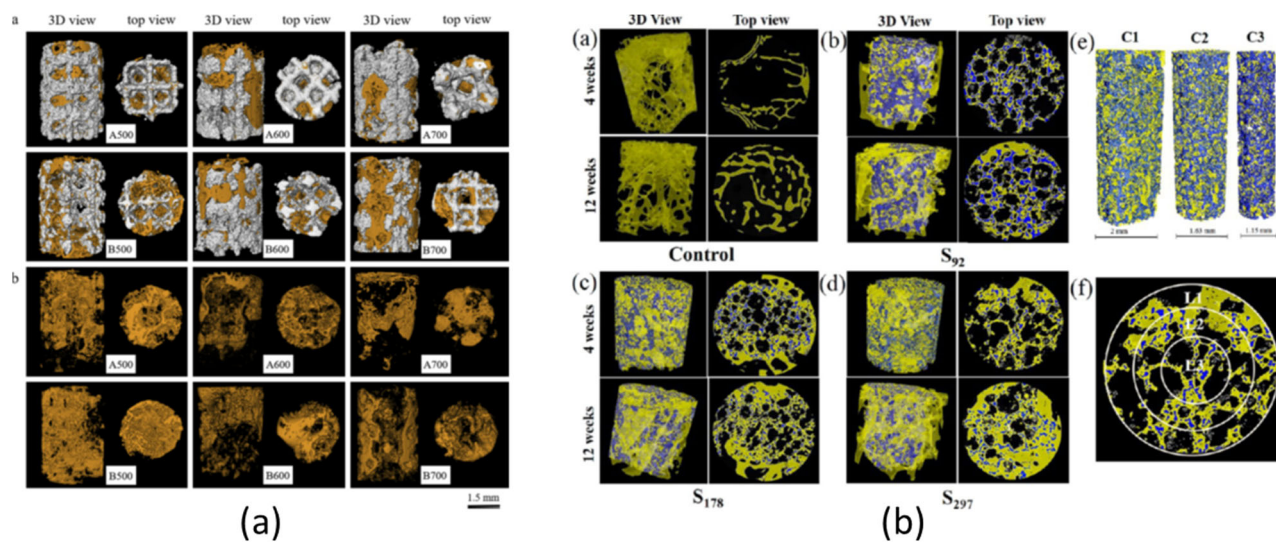

Figure 9. *Cont.*
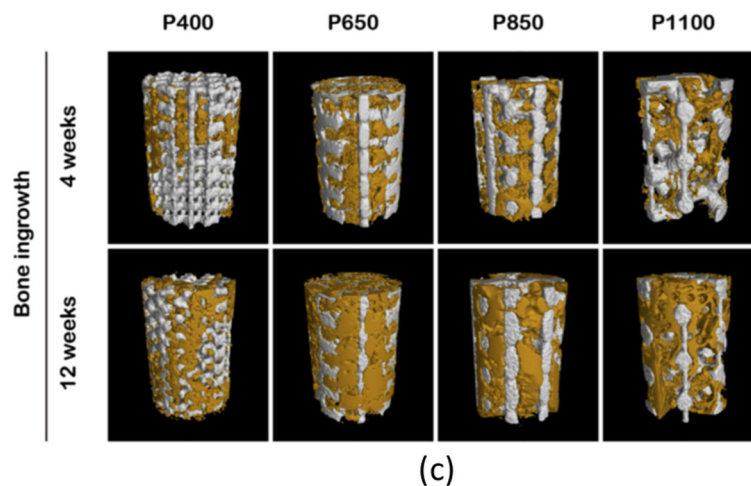
Figure 9. Quantitative μ-CT analysis of new bone ingrowth in the research papers of the following: (**a**) Chen et al. [96]; (**b**) Kapat et al. [92]; (**c**) Ouyang et al. [95].

In brief, porosity, pore size and pore interconnectivity are important factors influencing the mechanical and biological properties of scaffolds, bone ingrowth and the transportation of cells and nutrients. Given the discrepancy among findings, the optimal topological scaffold architecture remains a major challenge in biomedical applications.

4.2. Effect of Surface Roughness

Another factor affecting bone ingrowth is the surface roughness. Porous samples with highly rough surfaces, Ra $\geq$ 56.9 μm, resulted in a reduction in proliferation and bone ingrowth [98], while the surface roughness with range of 0.5 up to 8.5 μm positively influenced the bone implant [26]. Surface roughness affects the permeability of porous implants. As surface roughness increases, the permeability decreases. High values of permeability enhance the osteointegration process, since the transportation of cells, nutrients and growth factors requires the flow of blood through the porous scaffolds [99]. Chen et al. [100] manufactured Ti6Al4V discs with different additive angles, via an SLM process, with the aim of maximizing the direct effects of the additive angle on surface properties and biocompatibility. As the angle increases, the surface roughness increases because of the increasement of unmelted metallic particles. They, in vitro, evaluated the effect to osteoblast attachment and proliferation with six surface roughness values ranging from 2 to 3 μm, in comparison to those with wrought samples (see Figure 10).
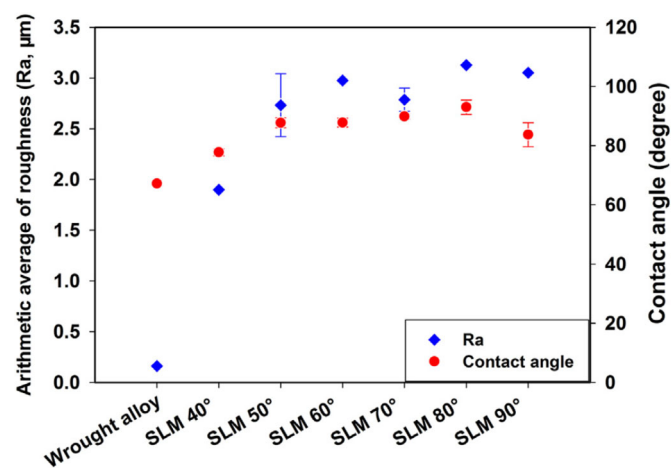
Figure 10. Arithmetic average roughness (Ra) and contact angle of wrought alloy and SLM-fabricated Ti6Al4V discs with different additive angles [100].

Adhesion and proliferation were found to be similar on the surface for every angle (see Figure 11), though cells initially adhered less with improved cell spreading at a higher additive angle.

(a)

(b)
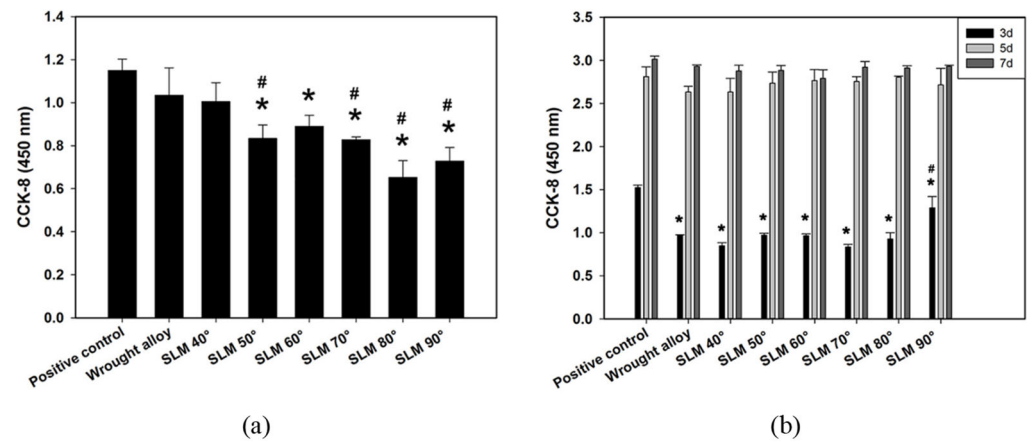
Figure 11. Cell (**a**) adhesion and (**b**) proliferation on wrought alloy and SLM-fabricated Ti6Al4V discs with different additive angles and surface roughness [100]. * indicates $p < 0.5$; # indicates $p < 0.01$.

Li et al. [101] prepared porous Ti6Al4V scaffolds via EBM; then, scaffolds were subjected to solution treatment at 800 °C, 950 °C and 1000 °C and then water quenching. Heat treatment increased surface roughness, obtaining values in the range of 3 up to 8 µm (see Figure 12).
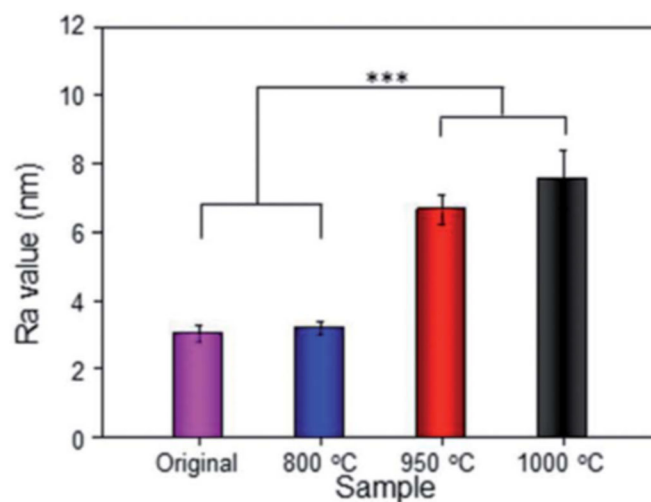
Figure 12. Ra values of original and heat-treated samples [101]. *** indicates $p < 0.5$.

The result showed that the scaffold heat treated at 1000 °C exhibited the best cellular adhesion and proliferation after in vitro culture (see Figure 13).
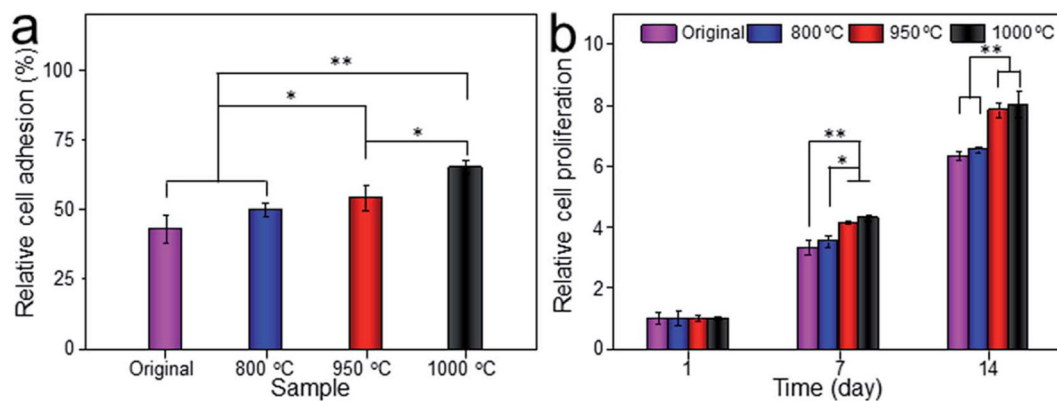
Figure 13. (**a**) Relative cell adhesion on the porous titanium cultured in vitro for 24 h; (**b**) relative cell proliferation on the porous titanium cultured in vitro for 1, 7 and 14 days [101]. * indicates $p < 0.5$; ** indicates $p < 0.01$.

4.3. Effect of Elastic Modulus

Implants made of metals and alloys are usually stiffer than human bone mechanical properties; specifically, the Ti6Al4V alloy has an elastic modulus of nearly 110 GPa [102,103]. Mechanical properties of bone vary significantly with age, bone quality and the presence of diseases [104]. The elastic modulus continues to cause a scientific challenge to fully understand the mechanics of living bones [67]. Cortical bone is stiffer when loaded longitudinally than in transverse and shear directions and presents a longitudinal modulus ranging from 18 to 20 GPa, transverse modulus between 10 and 12 GPa and shear modulus of around 3 GPa [105–108]. Cancellous bone presents a low elastic modulus, ranging from 0.2 to 4 GPa [105,108–110]. This mismatch in the elastic modulus may lead to stress shielding, which represents a major issue for bone resorption and eventual failure of the implants [19,111]. The internal lattice architecture, i.e., porosity, pore size and pore interconnectivity, can be designed to lower the equivalent elastic modulus of the implant, avoiding the mismatch between the stiffness of the implant and the adjacent bone [112]. This will allow the matching of mechanical requirements of the bone substitute to reduce the stress shielding by satisfying loading requirements. This may however avoid the mechanical failure of the implant [113], by maintaining an appropriate mechanical strength. Indeed, porous scaffolds also have a load-bearing function [114,115].

The choice of the most suitable lattice topology that should be used for the conception of biomedical implants is still controversial. Parisien et al. [59] investigated the capability of strut-based lattices to enhance osteointegration. They compared twenty-four lattice topologies with ten different relative densities, from 5 up to 50%, subjected to bone ingrowth stimulations by applying four different pressures, in the range of 0.5 to 2 MPa. They evaluated the effect of the lattice elastic modulus on the percentage of pores that is optimal for bone ingrowth. Relative densities lower than 20% showed similar bone ingrowth performance. For relative densities higher than 30%, at the lowest pressure of 0.5 MPa, topologies with a smaller elastic modulus stimulate better bone ingrowth, while at the highest pressure of 2 MPa, the FCCZ, which has the highest elastic modulus, was the only topology showing less than 70% of bone stimulation (see Figure 14). Since various topologies presented more than 90% of their optimal space, the authors assessed that topology choice can be based on the elastic modulus that fits the design's needs.
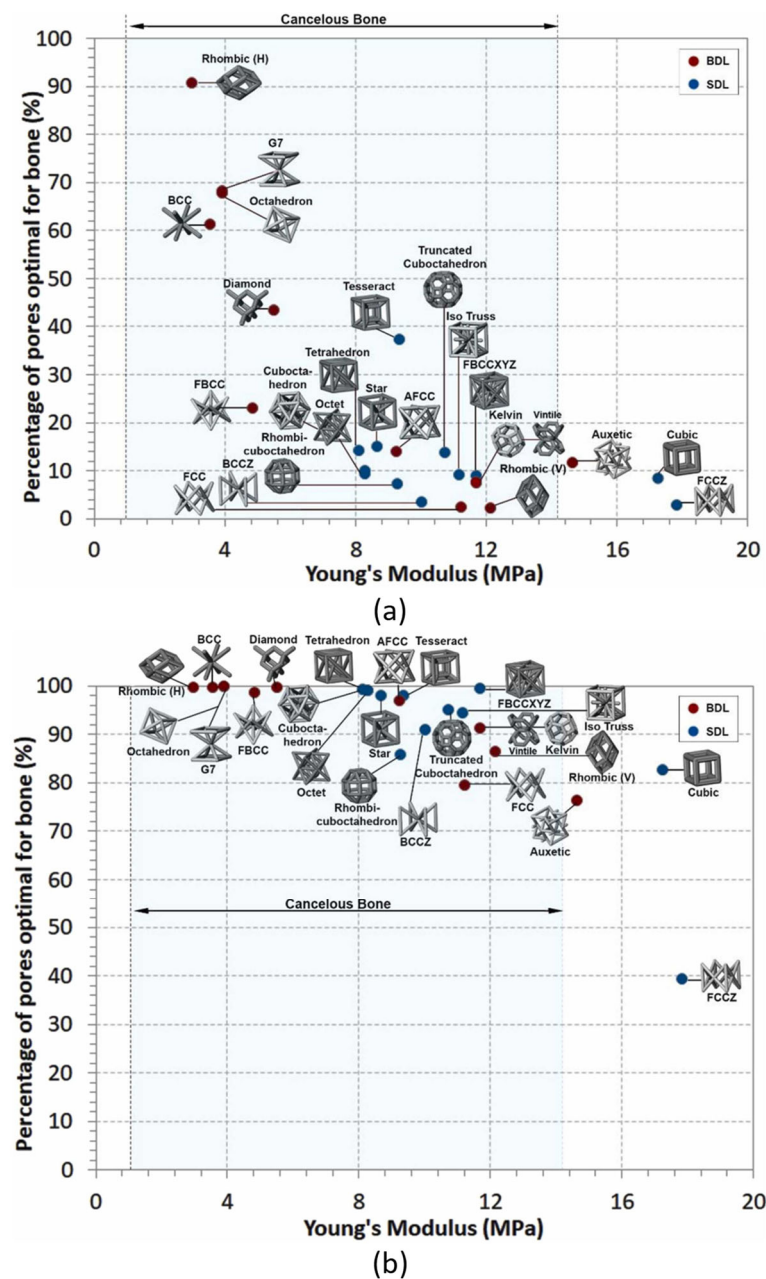
Figure 14. Percentage of pores optimal for bone ingrowth as a function of the elastic modulus under a pressure and a relative density of, respectively: (**a**) 0.5 MPa and 30%; (**b**) 2 MPa and 30% [59].

Several studies evaluated the effects of the elastic modulus of biomedical implants. Sun et al. [116] proposed a novel ZK60 cervical cage and evaluated the biomechanical properties under flexion, extension, lateral bending and axial rotation of the cervical spine. They performed cage optimization by decreasing the volume of 40% to reduce the cage's stiffness. They observed that the optimized cage can considerably enhance the stress stimulation of the bone by reducing the stress-shielding effect between the implant and vertebral bodies. They also observed that the stresses at the endplate–cage interface decrease while the cage's stiffness decreases, indicating that subsidence is less likely to occur in the device with lower stiffness. Wieding et al. [115] evaluated the mechanical performance of two types of Ti6Al4V-custom-made porous implants, with an elastic modulus of 6 and 8 GPa, implanted into a 20 mm segmental defect in the metatarsus of sheep. After 12 and 24 weeks postoperative, they performed torsional testing on the implanted bone and compared it to the contralateral non-treated side. Both types of implants offered mechanically stable

situations, with bone tissue ingrowth around and into the implants, presenting an elastic modulus in the range of the cortical bone.

5. The Gibson–Ashby Model

5.1. Compressive Behaviour

Lattice structure can be categorized based on its mechanical response as bending-dominated or stretch-dominated. Bending-dominated structures are compliant and absorb energy well when compressed; stretch-dominated structures have greater stiffness and compressive strength compared to bending-dominated lattices, for a given relative density [117].

Figure 15 shows the compressive stress–strain curve of a bending-dominated lattice.
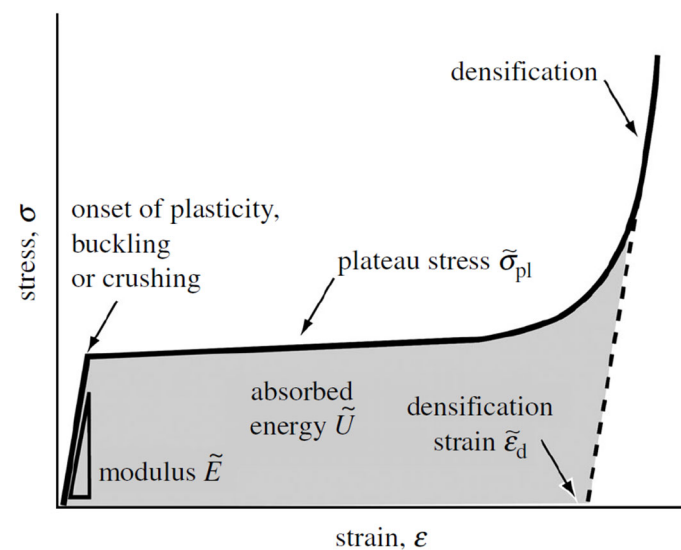

Figure 15. Stress–strain curve of a bending-dominated lattice [117].

The deformation behaviour can be divided into three stages: linear elastic deformation, plastic deformation and densification. In the first stage, the lattice material response is linear elastic with a Young's modulus proportional to the structure material compliance. Under compression, the struts of lattice materials are exposed to three mechanisms of collapse: yield, buckling or crushing. They compete until the mechanism with the lowest stress threshold is reached. Once the elastic limit is reached, plastic deformation begins and the structure keeps collapsing at a nearly constant stress, referred to as the plateau stress, until the opposite side of the cells impinge, constraining further deformation. The densification strain is reached, and densification begins as stress rises steeply [29,117].

When subjected to a tensile/compressive loading, a stretch-dominated lattice material first responds via elastic stretch of the struts; on average, in the first stage of the curve only one-third of lattice strut bears loads [117]. In this case, the elastic limit is reached when one or more sets of struts yield plastically, buckle or crush. Once the elastic limit is reached, the whole lattice material bears the loads, and the structure fails through strut fracture. The stretch-dominated mechanisms of deformation involve hard modes (stretching) compared to the soft ones (bending) of the bending-dominated structures; therefore, initial yielding is followed by plastic buckling or brittle collapse of the struts, leading to post-yield softening, with oscillation of the stress required for further deformation. Then, the densification strain is reached, and the stress steeply increases. Figure 16 shows the compressive stress–strain curve of a stretch-dominated lattice.
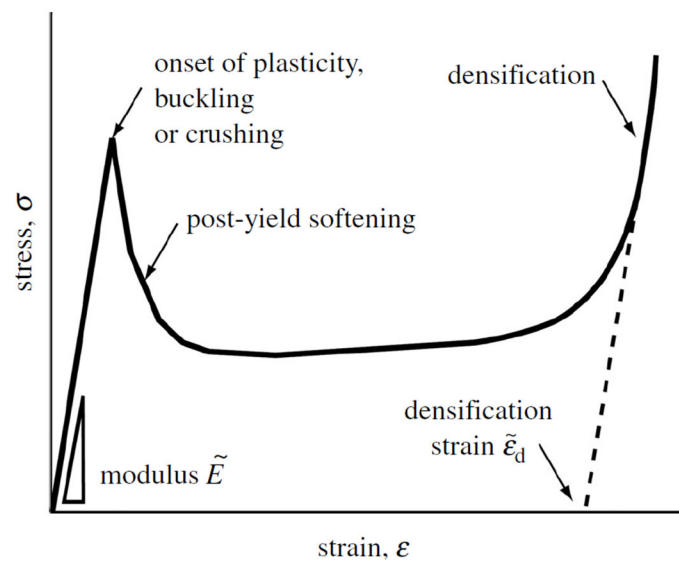
Figure 16. Stress–strain curve of a stretch-dominated lattice [117].

The deformation behaviour of strut-based topologies can be estimated by Maxwell's stability criterion, by evaluating the Maxwell number M of the lattice material.

$$M = S - 3N + 6 \tag{4}$$

If M < 0, the structure is bending dominated; if M ≥ 0, the structure is stretch dominated; if M > 0 the structure is hyperstatic [118].

The Maxwell number of most commonly studied strut-based unit cells is reported in Table 3.

Table 3. Maxwell number for strut-based unit cells.

Unit Cell Topology	Cubic	BCC	Diamond	Octet-Truss	TC	RD	RCO	TCO
S	12	8	9	36	36	24	48	72
N	8	9	7	14	24	14	24	48
M	−6	−13	−6	0	−30	−12	−18	−66

5.2. Comparison of Experimental Data for Different Lattice Materials

The Gibson–Ashby model is the most relevant and commonly recognized model for the prediction of the lattice's mechanical properties, which depend on the deformation behaviour exhibited by the structure (bending or stretch-dominated) and show a positive power relationship with the structure relative density. Gibson–Ashby provided the formulae relating the elastic modulus and strength of lattice structures to their relative density:

$$\frac{E^*}{E_s} = C_1 \left(\frac{\rho^*}{\rho_s} \right)^{n_1} \tag{5}$$

$$\frac{\sigma^*}{\sigma_s} = C_2 \left(\frac{\rho^*}{\rho_s} \right)^{n_2} \tag{6}$$

C_1, n_1, C_2 and n_2 are constant values dependent on the unit cell topology and are experimentally derived.

The n exponent can be predicted on the basis of the lattice deformation behaviour. In stretching-dominated structures, both stiffness and strength scale linearly as a function of the relative density and are higher than that of bending-dominated structures in which the elastic modulus scales quadratically with the relative density, while the strength scales with a factor of 3/2 [3].

The results of the experimental tests can be summarized in a graph in which the relative elastic modulus and relative strength are plotted against relative density (Figures 17 and 18). Through data interpolation, the constant values reported in Equations (5) and (6) can be calculated for a given lattice structure.
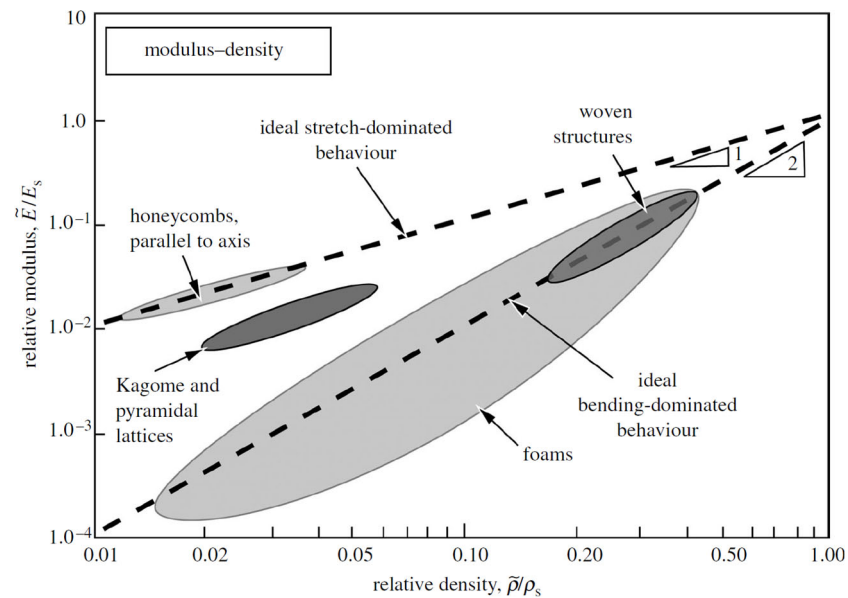
Figure 17. Gibson–Ashby model: relative modulus against relative density [117].
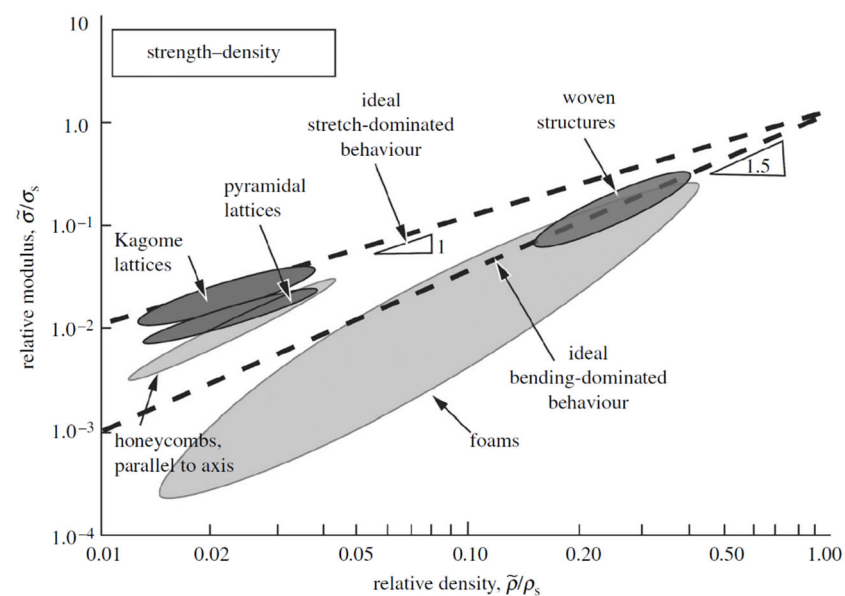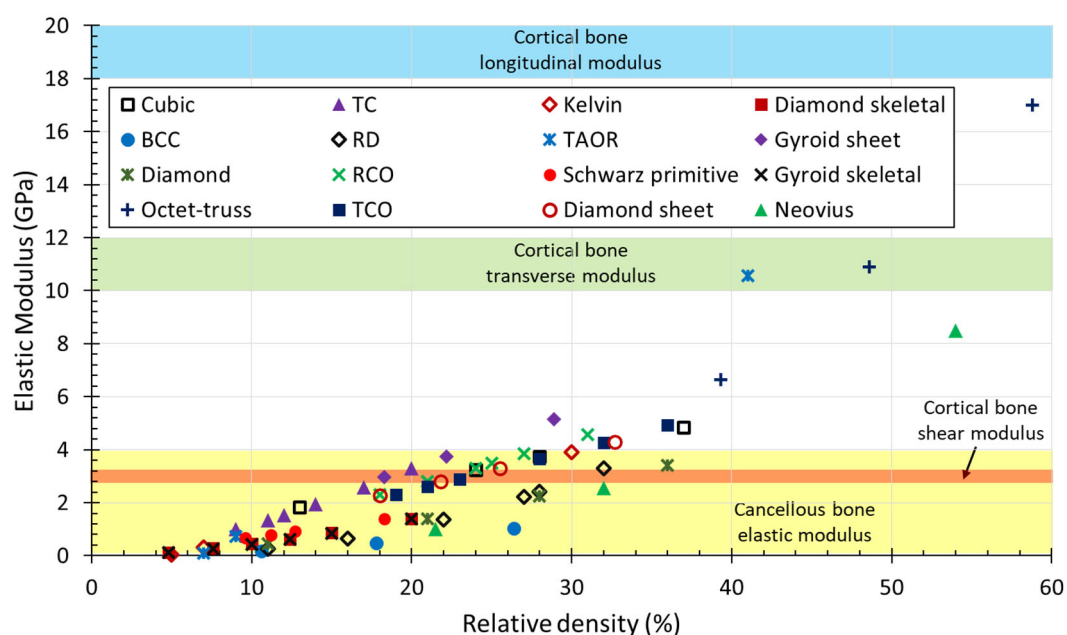

Figure 18. Gibson–Ashby model: relative strength against relative density [117].

Many studies performed on Ti6Al4V lattice materials are consistent with predictions obtained by the Gibson–Ashby model. Gibson–Ashby parameters from compressive tests, performed on different topologies and reported in the literature, were collected and are presented in Table 4.

Table 4. Gibson–Ashby model parameters from compressive tests reported in the literature.

Unit Cell Topology	Elastic Modulus (GPa)		Compressive Strength (MPa)	
	C_1	n_1	C_2	n_2
Cubic [35]	0.11	0.92	1.15	1.75
Cubic [119]	0.55	2.82	1.34	1.85
BCC [120]	0.15	2	0.57	1.9
BCC [121]	0.15	2	0.23	1.5
Diamond [118]	0.17	1.68	0.56	1.58
Octet-truss [119]	0.51	2.33	1.37	1.37
TC [118]	0.32	1.5	1.49	1.9
RD [118]	0.42	2.34	1.29	2.27
RD [122]	1.08	1.9	0.6	1.31
RCO [118]	0.17	1.25	0.97	1.62
TCO [118]	0.14	1.18	0.99	1.78
Kelvin [58]	0.6	2.3	0.3	1.5
TAOR [58]	0.8	2.3	0.6	1.5
Schwarz Primitive [123]	0.09	1.15	0.34	1.25
Schwarz Primitive [124]	1.38	2	0.98	1.5
Diamond Sheet [125]	0.71	1.21	0.42	1.14
Diamond Sheet [123]	0.12	1.06	1.66	1.89
Diamond Skeletal [15]	0.17	1.64	1.39	1.95
Diamond Skeletal [126]	0.7	2.7	1.17	2.6
Gyroid Sheet [127]	0.2	1.2	0.67	1.3
Gyroid Sheet [123]	0.12	1.1	2.07	2.03
Gyroid Skeletal [15]	0.19	1.71	1.31	1.83
Gyroid Skeletal [128]	0.29	2	0.46	1.5
Neovius [126]	0.31	2.3	1.43	2.9

Both the elastic modulus and compressive strength increase with the relative density. Collected experimental data were plotted in the Gibson–Ashby diagram to compare mechanical properties as a function of the relative density. Figure 19 shows the elastic modulus of the lattice structures, since the material used in the collected papers is the Ti6Al4V alloy in all cases. Therefore, the elastic modulus of the lattice materials can be compared to that of human bone. Figure 20 shows the relative strength against the relative density.

Figure 19. Comparison of the collected experimental data in the Gibson–Ashby diagram: elastic modulus against relative density.
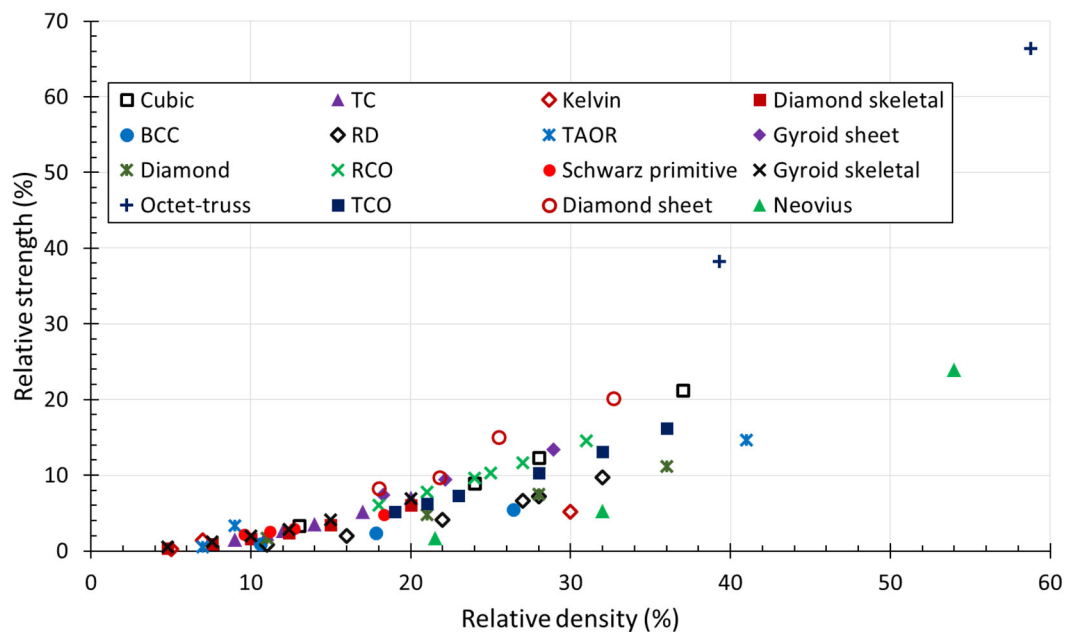
Figure 20. Comparison of the collected experimental data in the Gibson–Ashby diagram: relative strength against relative density.

6. Biomedical Device Case Studies

Ti6Al4V porous device performances are widely examined via in silico, in vitro and in vivo experiments. Ti6Al4V scaffolds are applied for the treatment of bone disorders in the mandible, shoulder, spine, hip and femur.

Gao et al. [129] investigated and optimized, by employing finite element analysis (FEA) and the bone "Mechnostat" theory, porous scaffolds for mandibular defects. They considered both the biomechanical behaviour and mechanobiological property of scaffolds and analysed four lattice configurations with three strut diameters. The results showed a strong correlation between lattice topology and load transmission capacity, while mechanical failure strongly depends on the strut size and configuration; moreover, the computational model results indicated that the optimized scaffold can provide an excellent mechanical environment for bone regeneration. Liu et al. [130] compared conventional prostheses with homogeneous structures to stress-optimized functionally graded devices. They investigated, in silico, the damage resistance of four scaffolds and proposed a novel gradient algorithm for lightweight mandibular devices. The results illustrated that the optimized device reduced the maximum stress by 24.48% and increased the porosity by 6.82%, providing a better solution for mandibular reconstruction.

Bittredge et al. [131] investigated the stress shielding of total shoulder implants. The purpose of the study was the design and optimization of a lattice-based implant to manage the stiffness of a humeral implant stem used in shoulder implant applications. The study applied a topology lattice-optimization tool to develop various cellular designs that filled the original design of a shoulder implant and were further analysed by means of FEA and experimental tests. The results indicated that the proposed cellular implant can be effectively applied as a total shoulder replacement.

Fogel et al. [132] applied in vitro testing to elucidate the relative contribution of a porous design to intervertebral device stiffness and subsidence performance. Four groups of titanium cages were created with a combination of a porous endplate and/or an internal lattice architecture. The cage stiffness was scaled down by 16.7% by the internal lattice architecture and by 16.6% by the porous endplates. The cage with both porous parts exhibited the lowest stiffness with a value of 40.4 kN/mm and a motion segment stiffness of 1976.8 N/mm for subsidence. The internal lattice architecture showed no significant impact on the motion segment stiffness, while the porous endplates significantly decreased

this value. Several works evaluated, using computed tomography (CT), the fusion rate of Ti6Al4V cages and PEEK cages by comparing groups of patients who had undergone cage implantation. Cuzzocrea et al. [133] found a better fusion rate and prevalence of fusion in the group treated with Ti6Al4V cages. Nemoto et al. [134] found a 96% fusion rate in the Ti6Al4V group and 64% in the PEEK group after 12 months. At 24 months, the fusion rate in the Ti6Al4V group was increased to 100%, while that in the PEEK group showed a 76% fusion rate. They also observed vertebral osteolysis in 60% of the cases with non-union in the PEEK group. This unusual finding was not observed in the Ti6Al4V group. Tanida et al. [135] observed a postoperative bone union rate of 75.2% and 74.5% at 1 year and 82.8% and 80.4% at 2 years for Ti6Al4V and PEEK groups, respectively, concluding that the bone union rate did not significantly differ between the two groups. They reported that the formation of vertebral endplate cysts is helpful for the non-union prediction, confirming after CT scan observations, the usefulness of this parameter.

Abate et al. [56] focused on the design of an acetabular cup using vintile lattice material with different porosities and pore sizes. The acetabular cup was then optimized by adjusting the porosity to improve mechanical performance and reduce stress shielding. In silico and in vitro experiments were carried out, and results showed that the optimized implant presents a weight reduction of 69%, reduced the stress shielding, has a more uniform stress distribution and has an elastic modulus in the range of that of human bones.

Gok [136] developed a multi-lattice design by dividing the proximal zone of a hip implant stem into three parts. Due to the multi-lattice design, a weight reduction of 25.89% was obtained and the maximum von Mises stresses in the stem were reduced from 289 to 189 MPa. They obtained stress shielding signals by determining the change in strain energy per unit bone mass caused by the presence of the femoral hip implant stem and its ratio to intact bone. In the case of multi-lattice design implants, there is a significant increase in stress-shielding signals from different zones of the femur.

7. Concluding Remarks

Progress in AM has considerably increased the production of complex structures unachievable with traditional fabrication techniques, such as lattice structures. This has led to research into these structures for different engineering applications. In the biomedical field, lattice materials made of Ti6Al4V alloy are widely used for the fabrication of scaffolds for bone substitutes. This review collected the most significant findings of the last ten years, which are summarized as follows:

- Data analysis of the results of the pore size effect on the bone ingrowth of eleven studies showed a wide range of optimal pore sizes from 100 up to 1000 μm, with an optimal mean value of 522 μm. The comparison showed little discrepancies, since works that evaluated comparable ranges of pore sizes found different optimal results.
- The analysis of the effect of surface roughness showed that minimal differences in the roughness values do not affect the cell adhesion and proliferation. In other studies, the comparison of a wide range values from 3 to 8 μm showed that the optimal surface roughness values are between 6 and 8 μm.
- Findings on the effect of the elastic modulus showed that reducing the implant stiffness to that of human bone improves stress stimulation and reduces stress shielding. Several studies with implants having an elastic modulus comparable to that of human bone revealed no significant influence of elastic material properties on bone ingrowth.
- The Gibson–Ashby model is useful for comparing the mechanical performance of lattice structures and confirmed the suitability of the Ti6Al4V alloy for biomedical applications. Indeed, the collected results showed that the elastic modulus of the selected lattice materials, with relative densities under 30%, falls within the range of the cancellous bone elastic modulus.

Future works include the development of a repeatable and robust design methodology of biomedical implants with a combination of Gibson–Ashby model data and in silico and

in vitro experiments. Data reported in the present review provide a scientific base for the choice of the optimal lattice topology and design parameters.

Nomenclature

TPMS	triply periodic minimal surface
AM	additive manufacturing
SLM	selective laser melting
SLS	selective laser sintering
DMLS	direct metal laser sintering
EBM	electron beam melting
BCC	body-centred cubic
FCC	face-centred cubic
BCCZ	body-centred cubic with vertical struts
FCCZ	face-centred cubic with vertical struts
SCBCC	simple cubic body-centred cubic
TC	truncated cube
TO	truncated octahedron
RCO	rhombicuboctahedron
TCO	truncated cuboctahedron
RD	rhombic dodecahedron
TAOR	triply arranged octagonal rings
τ	complex variable
θ	Bonnet angle
$R(\tau)$	TPMS function
γ	position vector in the Euclidean space
A_k	amplitude factor
h_k	k_{th} grid vector in the reciprocal space
λ_k	periodic wavelength
p_k	phase offset
C	constant factor related to porosity
M	Maxwell number
S	number of struts
N	number of nodes
E^*	elastic modulus of the lattice structure
σ^*	compressive strength of the lattice structure
E_s	elastic modulus of the parent material
σ_s	compressive strength of the parent material
FEA	finite element analysis
PEEK	polyetheretherketone
CT	computed tomography

References

1. Zadpoor, A.A. Mechanical Performance of Additively Manufactured Meta-Biomaterials. *Acta Biomater.* **2019**, *85*, 41–59. [CrossRef]
2. Gibson, L.J.; Ashby, M.F. *Cellular Solids—Structure and Properties*; Cambridge University Press: Cambridge, UK, 1997.
3. Al-Ketan, O.; Rowshan, R.; Abu Al-Rub, R.K. Topology-Mechanical Property Relationship of 3D Printed Strut, Skeletal, and Sheet Based Periodic Metallic Cellular Materials. *Addit. Manuf.* **2018**, *19*, 167–183. [CrossRef]
4. Ngo, T.D.; Kashani, A.; Imbalzano, G.; Nguyen, K.T.Q.; Hui, D. Additive Manufacturing (3D Printing): A Review of Materials, Methods, Applications and Challenges. *Compos. Part B Eng.* **2018**, *143*, 172–196. [CrossRef]

5. Huang, Y.; Leu, M.C.; Mazumder, J.; Donmez, A. Additive Manufacturing: Current State, Future Potential, Gaps and Needs, and Recommendations. *J. Manuf. Sci. Eng.* **2015**, *137*, 014001. [CrossRef]

6. Bhushan, S.; Singh, S.; Maiti, T.K.; Sharma, C.; Dutt, D.; Sharma, S.; Li, C.; Tag Eldin, E.M. Scaffold Fabrication Techniques of Biomaterials for Bone Tissue Engineering: A Critical Review. *Bioengineering* **2022**, *9*, 728. [CrossRef] [PubMed]

7. Louvis, E.; Fox, P.; Sutcliffe, C.J. Selective Laser Melting of Aluminium Components. *J. Mater. Process. Technol.* **2011**, *211*, 275–284. [CrossRef]

8. Mazzoli, A. Selective Laser Sintering in Biomedical Engineering. *Med. Biol. Eng. Comput.* **2013**, *51*, 245–256. [CrossRef]

9. Simchi, A.; Petzoldt, F.; Pohl, H. On the Development of Direct Metal Laser Sintering for Rapid Tooling. *J. Mater. Process. Technol.* **2003**, *141*, 319–328. [CrossRef]

10. Körner, C. Additive Manufacturing of Metallic Components by Selective Electron Beam Melting—A Review. *Int. Mater. Rev.* **2016**, *61*, 361–377. [CrossRef]

11. Maconachie, T.; Leary, M.; Tran, P.; Harris, J.; Liu, Q.; Lu, G.; Ruan, D.; Faruque, O.; Brandt, M. The Effect of Topology on the Quasi-Static and Dynamic Behaviour of SLM AlSi10Mg Lattice Structures. *Int. J. Adv. Manuf. Technol.* **2022**, *118*, 4085–4104. [CrossRef]

12. Kim, T.; Zhao, C.Y.; Lu, T.J.; Hodson, H.P. Convective Heat Dissipation with Lattice-Frame Materials. *Mech. Mater.* **2004**, *36*, 767–780. [CrossRef]

13. du Plessis, A.; Yadroitsava, I.; Yadroitsev, I.; le Roux, S.G.; Blaine, D.C. Numerical Comparison of Lattice Unit Cell Designs for Medical Implants by Additive Manufacturing. *Virtual Phys. Prototyp.* **2018**, *13*, 266–281. [CrossRef]

14. Vilardell, A.M.; Takezawa, A.; du Plessis, A.; Takata, N.; Krakhmalev, P.; Kobashi, M.; Yadroitsava, I.; Yadroitsev, I. Topology Optimization and Characterization of Ti6Al4V ELI Cellular Lattice Structures by Laser Powder Bed Fusion for Biomedical Applications. *Mater. Sci. Eng. A* **2019**, *766*, 138330. [CrossRef]

15. Yan, C.; Hao, L.; Hussein, A.; Young, P. Ti-6Al-4V Triply Periodic Minimal Surface Structures for Bone Implants Fabricated via Selective Laser Melting. *J. Mech. Behav. Biomed. Mater.* **2015**, *51*, 61–73. [CrossRef] [PubMed]

16. Caiazzo, F.; Alfieri, V.; Bujazha, B.D. Additive Manufacturing of Biomorphic Scaffolds for Bone Tissue Engineering. *Int. J. Adv. Manuf. Technol.* **2021**, *113*, 2909–2923. [CrossRef]

17. Liu, X.; Chu, P.K.; Ding, C. Surface Modification of Titanium, Titanium Alloys, and Related Materials for Biomedical Applications. *Mater. Sci. Eng. R Rep.* **2004**, *47*, 49–121. [CrossRef]

18. Abdel-Hady Gepreel, M.; Niinomi, M. Biocompatibility of Ti-Alloys for Long-Term Implantation. *J. Mech. Behav. Biomed. Mater.* **2013**, *20*, 407–415. [CrossRef]

19. Long, M.; Rack, H.J. Titanium Alloys in Total Joint Replacement—A Materials Science Perspective. *Biomaterials* **1998**, *19*, 1621–1639. [CrossRef]

20. Petersen, A.; Joly, P.; Bergmann, C.; Korus, G.; Duda, G.N. The Impact of Substrate Stiffness and Mechanical Loading on Fibroblast-Induced Scaffold Remodeling. *Tissue Eng. Part A* **2012**, *18*, 1804–1817. [CrossRef]

21. Breuls, R.G.M.; Jiya, T.U.; Smit, T.H. Scaffold Stiffness Influences Cell Behavior: Opportunities for Skeletal Tissue Engineering. *Open Orthop. J.* **2008**, *2*, 103. [CrossRef] [PubMed]

22. Rack, H.J.; Qazi, J.I. Titanium Alloys for Biomedical Applications. *Mater. Sci. Eng. C* **2006**, *26*, 1269–1277. [CrossRef]

23. Li, F.; Li, J.; Xu, G.; Liu, G.; Kou, H.; Zhou, L. Fabrication, Pore Structure and Compressive Behavior of Anisotropic Porous Titanium for Human Trabecular Bone Implant Applications. *J. Mech. Behav. Biomed. Mater.* **2015**, *46*, 104–114. [CrossRef] [PubMed]

24. Chang, B.; Song, W.; Han, T.; Yan, J.; Li, F.; Zhao, L.; Kou, H.; Zhang, Y. Influence of Pore Size of Porous Titanium Fabricated by Vacuum Diffusion Bonding of Titanium Meshes on Cell Penetration and Bone Ingrowth. *Acta Biomater.* **2016**, *33*, 311–321. [CrossRef]

25. Rnjak-Kovacina, J.; Wise, S.G.; Li, Z.; Maitz, P.K.M.; Young, C.J.; Wang, Y.; Weiss, A.S. Tailoring the Porosity and Pore Size of Electrospun Synthetic Human Elastin Scaffolds for Dermal Tissue Engineering. *Biomaterials* **2011**, *32*, 6729–6736. [CrossRef] [PubMed]

26. Shalabi, M.M.; Gortemaker, A.; Van't Hof, M.A.; Jansen, J.A.; Creugers, N.H.J. Implant Surface Roughness and Bone Healing: A Systematic Review. *J. Dent. Res.* **2006**, *85*, 496–500. [CrossRef] [PubMed]

27. Krishna Alla, R.; Ginjupalli, K.; Upadhya, N.; Shammas, M.; Krishna Ravi, R.; Sekhar, R. Surface Roughness of Implants: A Review. *Trends Biomater. Artif. Organs* **2011**, *25*, 112–118.

28. Gibson, L.J.; Ashby, M.F. Mechanics of Three-Dimensional Cellular Materials. *Proc. R. Soc. Lond. A. Math. Phys. Sci.* **1982**, *382*, 43–59. [CrossRef]

29. Maconachie, T.; Leary, M.; Lozanovski, B.; Zhang, X.; Qian, M.; Faruque, O.; Brandt, M. SLM Lattice Structures: Properties, Performance, Applications and Challenges. *Mater. Des.* **2019**, *183*, 108137. [CrossRef]

30. Deshpande, V.S.; Fleck, N.A.; Ashby, M.F. Effective Properties of the Octet-Truss Lattice Material. *J. Mech. Phys. Solids* **2001**, *49*, 1747–1769. [CrossRef]

31. Peng, C.; Tran, P.; Nguyen-Xuan, H.; Ferreira, A.J.M. Mechanical Performance and Fatigue Life Prediction of Lattice Structures: Parametric Computational Approach. *Compos. Struct.* **2020**, *235*, 111821. [CrossRef]

32. Wu, M.W.; Chen, J.K.; Lin, B.H.; Chiang, P.H.; Tsai, M.K. Compressive Fatigue Properties of Additive-Manufactured Ti-6Al-4V Cellular Material with Different Porosities. *Mater. Sci. Eng. A* **2020**, *790*, 139695. [CrossRef]

33. Chen, J.K.; Wu, M.W.; Cheng, T.L.; Chiang, P.H. Continuous Compression Behaviors of Selective Laser Melting Ti-6Al-4V Alloy with Cuboctahedron Cellular Structures. *Mater. Sci. Eng. C* **2019**, *100*, 781–788. [CrossRef] [PubMed]

34. Hedayati, R.; Sadighi, M.; Mohammadi-Aghdam, M.; Zadpoor, A.A. Mechanical Properties of Regular Porous Biomaterials Made from Truncated Cube Repeating Unit Cells: Analytical Solutions and Computational Models. *Mater. Sci. Eng. C* **2016**, *60*, 163–183. [CrossRef] [PubMed]

35. Ahmadi, S.M.; Yavari, S.A.; Wauthle, R.; Pouran, B.; Schrooten, J.; Weinans, H.; Zadpoor, A.A. Additively Manufactured Open-Cell Porous Biomaterials Made from Six Different Space-Filling Unit Cells: The Mechanical and Morphological Properties. *Materials* **2015**, *8*, 1871–1896. [CrossRef]

36. Guerra Silva, R.; Salinas Estay, C.; Morales Pavez, G.; Torres, M.J.; Zahr Viñuela, J. Assessment of Analytical Relationships for Mechanical Properties of Truncated Octahedron and Diamond Lattice Structures. *Mater. Today Commun.* **2021**, *29*, 102756. [CrossRef]

37. Qi, D.; Yu, H.; Liu, M.; Huang, H.; Xu, S.; Xia, Y.; Qian, G.; Wu, W. Mechanical Behaviors of SLM Additive Manufactured Octet-Truss and Truncated-Octahedron Lattice Structures with Uniform and Taper Beams. *Int. J. Mech. Sci.* **2019**, *163*, 105091. [CrossRef]

38. Hedayati, R.; Sadighi, M.; Mohammadi-Aghdam, M.; Zadpoor, A.A. Mechanics of Additively Manufactured Porous Biomaterials Based on the Rhombicuboctahedron Unit Cell. *J. Mech. Behav. Biomed. Mater.* **2016**, *53*, 272–294. [CrossRef] [PubMed]

39. Hedayati, R.; Sadighi, M.; Mohammadi-Aghdam, M.; Zadpoor, A.A. Mechanical Behavior of Additively Manufactured Porous Biomaterials Made from Truncated Cuboctahedron Unit Cells. *Int. J. Mech. Sci.* **2016**, *106*, 19–38. [CrossRef]

40. Xiao, L.; Song, W. Additively-Manufactured Functionally Graded Ti-6Al-4V Lattice Structures with High Strength under Static and Dynamic Loading: Experiments. *Int. J. Impact. Eng.* **2018**, *111*, 255–272. [CrossRef]

41. Ma, S.; Song, K.; Lan, J.; Ma, L. Biological and Mechanical Property Analysis for Designed Heterogeneous Porous Scaffolds Based on the Refined TPMS. *J. Mech. Behav. Biomed. Mater.* **2020**, *107*, 103727. [CrossRef]

42. Michielsen, K.; Kole, S. Photonic Band Gaps in Materials with Triply Periodic Surfaces and Related Tubular Structures. *Phys. Rev. B* **2003**, *68*, 115107. [CrossRef]

43. Khaleghi, S.; Dehnavi, F.N.; Baghani, M.; Safdari, M.; Wang, K.; Baniassadi, M. On the Directional Elastic Modulus of the TPMS Structures and a Novel Hybridization Method to Control Anisotropy. *Mater. Des.* **2021**, *210*, 110074. [CrossRef]

44. Yang, E.; Leary, M.; Lozanovski, B.; Downing, D.; Mazur, M.; Sarker, A.; Khorasani, A.M.; Jones, A.; Maconachie, T.; Bateman, S.; et al. Effect of Geometry on the Mechanical Properties of Ti-6Al-4V Gyroid Structures Fabricated via SLM: A Numerical Study. *Mater. Des.* **2019**, *184*, 108165. [CrossRef]

45. Ataee, A.; Li, Y.; Fraser, D.; Song, G.; Wen, C. Anisotropic Ti-6Al-4V Gyroid Scaffolds Manufactured by Electron Beam Melting (EBM) for Bone Implant Applications. *Mater. Des.* **2018**, *137*, 345–354. [CrossRef]

46. Maszybrocka, J.; Gapiński, B.; Dworak, M.; Skrabalak, G.; Stwora, A. The Manufacturability and Compression Properties of the Schwarz Diamond Type Ti6Al4V Cellular Lattice Fabricated by Selective Laser Melting. *Int. J. Adv. Manuf. Technol.* **2019**, *105*, 3411–3425. [CrossRef]

47. Kadkhodapour, J.; Montazerian, H.; Darabi, A.C.; Zargarian, A.; Schmauder, S. The Relationships between Deformation Mechanisms and Mechanical Properties of Additively Manufactured Porous Biomaterials. *J. Mech. Behav. Biomed. Mater.* **2017**, *70*, 28–42. [CrossRef]

48. Li, Z.; Chen, Z.; Chen, X.; Zhao, R. Effect of Unit Configurations and Parameters on the Properties of Ti–6Al–4V Unit-Stacked Scaffolds: A Trade-off between Mechanical and Permeable Performance. *J. Mech. Behav. Biomed. Mater.* **2021**, *116*, 104332. [CrossRef] [PubMed]

49. Guo, X.; Ding, J.; Li, X.; Qu, S.; Song, X.; Fuh, J.Y.H.; Lu, W.F.; Zhai, W. Enhancement in the Mechanical Behaviour of a Schwarz Primitive Periodic Minimal Surface Lattice Structure Design. *Int. J. Mech. Sci.* **2022**, *216*, 106977. [CrossRef]

50. Lee, D.W.; Khan, K.A.; Abu Al-Rub, R.K. Stiffness and Yield Strength of Architectured Foams Based on the Schwarz Primitive Triply Periodic Minimal Surface. *Int. J. Plast.* **2017**, *95*, 1–20. [CrossRef]

51. Gao, T.; Liu, K.; Wang, X.; Li, Z.; Wang, Z. Elastic Mechanical Property Hybridization of Configuration-Varying TPMS with Geometric Continuity. *Mater. Des.* **2022**, *221*, 110995. [CrossRef]

52. Khan, K.A.; Abu Al-Rub, R.K. Time Dependent Response of Architectured Neovius Foams. *Int. J. Mech. Sci.* **2017**, *126*, 106–119. [CrossRef]

53. Dalaq, A.S.; Abueidda, D.W.; Abu Al-Rub, R.K.; Jasiuk, I.M. Finite Element Prediction of Effective Elastic Properties of Interpenetrating Phase Composites with Architectured 3D Sheet Reinforcements. *Int. J. Solids Struct.* **2016**, *83*, 169–182. [CrossRef]

54. Dong, G.; Zhao, Y.F. Numerical and Experimental Investigation of the Joint Stiffness in Lattice Structures Fabricated by Additive Manufacturing. *Int. J. Mech. Sci.* **2018**, *148*, 475–485. [CrossRef]

55. Abate, K.M.; Nazir, A.; Yeh, Y.P.; Chen, J.E.; Jeng, J.Y. Design, Optimization, and Validation of Mechanical Properties of Different Cellular Structures for Biomedical Application. *Int. J. Adv. Manuf. Technol.* **2020**, *106*, 1253–1265. [CrossRef]

56. Abate, K.M.; Nazir, A.; Chen, J.E.; Jeng, J.Y. Design, Optimization, and Evaluation of Additively Manufactured Vintiles Cellular Structure for Acetabular Cup Implant. *Processes* **2020**, *8*, 25. [CrossRef]

57. Alomar, Z.; Concli, F. Compressive Behavior Assessment of a Newly Developed Circular Cell-Based Lattice Structure. *Mater. Des.* **2021**, *205*, 109716. [CrossRef]

58. Distefano, F.; Mineo, R.; Epasto, G. Mechanical Behaviour of a Novel Biomimetic Lattice Structure for Bone Scaffold. *J. Mech. Behav. Biomed. Mater.* **2023**, *138*, 105656. [CrossRef]

59. Parisien, A.; ElSayed, M.S.A.; Frei, H. Mechanoregulation Modelling of Stretching versus Bending Dominated Periodic Cellular Solids. *Mater. Today Commun.* **2022**, *33*, 104315. [CrossRef]

60. Ghouse, S.; Babu, S.; van Arkel, R.J.; Nai, K.; Hooper, P.A.; Jeffers, J.R.T. The Influence of Laser Parameters and Scanning Strategies on the Mechanical Properties of a Stochastic Porous Material. *Mater. Des.* **2017**, *131*, 498–508. [CrossRef]

61. Gao, W.; Zhang, Y.; Ramanujan, D.; Ramani, K.; Chen, Y.; Williams, C.B.; Wang, C.C.L.; Shin, Y.C.; Zhang, S.; Zavattieri, P.D. The Status, Challenges, and Future of Additive Manufacturing in Engineering. *CAD Comput. Aided Des.* **2015**, *69*, 65–89. [CrossRef]

62. Lin, K.; Yuan, L.; Gu, D. Influence of Laser Parameters and Complex Structural Features on the Bio-Inspired Complex Thin-Wall Structures Fabricated by Selective Laser Melting. *J. Mater. Process. Technol.* **2019**, *267*, 34–43. [CrossRef]

63. Sachs, E.M. Powder Dispensing Apparatus Using Vibration. U.S. Patent No. 6,036,777, 14 May 2000. Washington, DC: U.S. Patent and Trademark Office.

64. Zhang, L.; Zhang, S.; Zhu, H.; Hu, Z.; Wang, G.; Zeng, X. Horizontal Dimensional Accuracy Prediction of Selective Laser Melting. *Mater. Des.* **2018**, *160*, 9–20. [CrossRef]

65. Nawada, S.; Dimartino, S.; Fee, C. Dispersion Behavior of 3D-Printed Columns with Homogeneous Microstructures Comprising Differing Element Shapes. *Chem. Eng. Sci.* **2017**, *164*, 90–98. [CrossRef]

66. Abdulhameed, O.; Al-Ahmari, A.; Ameen, W.; Mian, S.H. Additive Manufacturing: Challenges, Trends, and Applications. *Adv. Mech. Eng.* **2019**, *11*. [CrossRef]

67. Wang, X.; Xu, S.; Zhou, S.; Xu, W.; Leary, M.; Choong, P.; Qian, M.; Brandt, M.; Xie, Y.M. Topological Design and Additive Manufacturing of Porous Metals for Bone Scaffolds and Orthopaedic Implants: A Review. *Biomaterials* **2016**, *83*, 127–141. [CrossRef]

68. Abbasi, N.; Hamlet, S.; Love, R.M.; Nguyen, N.T. Porous Scaffolds for Bone Regeneration. *J. Sci. Adv. Mater. Devices* **2020**, *5*, 1–9. [CrossRef]

69. Bose, S.; Vahabzadeh, S.; Bandyopadhyay, A. Bone Tissue Engineering Using 3D Printing. *Mater. Today* **2013**, *16*, 496–504. [CrossRef]

70. Mayfield, C.K.; Ayad, M.; Lechtholz-Zey, E.; Chen, Y.; Lieberman, J.R. 3D-Printing for Critical Sized Bone Defects: Current Concepts and Future Directions. *Bioengineering* **2022**, *9*, 680. [CrossRef]

71. Abdulmaged, A.I.; Soon, C.F.; Talip, B.A.; Zamhuri, S.A.A.; Mostafa, S.A.; Zhou, W. Characterization of Alginate–Gelatin–Cholesteryl Ester Liquid Crystals Bioinks for Extrusion Bioprinting of Tissue Engineering Scaffolds. *Polymers* **2022**, *14*, 1021. [CrossRef] [PubMed]

72. Harrysson, O.L.A.; Cansizoglu, O.; Marcellin-Little, D.J.; Cormier, D.R.; West, H.A. Direct Metal Fabrication of Titanium Implants with Tailored Materials and Mechanical Properties Using Electron Beam Melting Technology. *Mater. Sci. Eng. C* **2008**, *28*, 366–373. [CrossRef]

73. Kolken, H.M.A.; de Jonge, C.P.; van der Sloten, T.; Garcia, A.F.; Pouran, B.; Willemsen, K.; Weinans, H.; Zadpoor, A.A. Additively Manufactured Space-Filling Meta-Implants. *Acta Biomater.* **2021**, *125*, 345–357. [CrossRef] [PubMed]

74. Liverani, E.; Rogati, G.; Pagani, S.; Brogini, S.; Fortunato, A.; Caravaggi, P. Mechanical Interaction between Additive-Manufactured Metal Lattice Structures and Bone in Compression: Implications for Stress Shielding of Orthopaedic Implants. *J. Mech. Behav. Biomed. Mater.* **2021**, *121*, 104608. [CrossRef] [PubMed]

75. Pei, X.; Wu, L.; Lei, H.; Zhou, C.; Fan, H.; Li, Z.; Zhang, B.; Sun, H.; Gui, X.; Jiang, Q.; et al. Fabrication of Customized Ti6Al4V Heterogeneous Scaffolds with Selective Laser Melting: Optimization of the Architecture for Orthopedic Implant Applications. *Acta Biomater.* **2021**, *126*, 485–495. [CrossRef]

76. Epasto, G.; Distefano, F.; Mineo, R.; Guglielmino, E. Subject-Specific Finite Element Analysis of a Lumbar Cage Produced by Electron Beam Melting. *Med. Biol. Eng. Comput.* **2019**, *57*, 2771–2781. [CrossRef] [PubMed]

77. Günther, F.; Wagner, M.; Pilz, S.; Gebert, A.; Zimmermann, M. Design Procedure for Triply Periodic Minimal Surface Based Biomimetic Scaffolds. *J. Mech. Behav. Biomed. Mater.* **2022**, *126*, 104871. [CrossRef]

78. Cucinotta, F.; Mineo, R.; Raffaele, M.; Salmeri, F.; Sfravara, F. Customized Implant of Cervical Prostheses Exploiting a Predictive Analysis of Range of Motion. *Comput. Aided Des. Appl.* **2023**, *20*, 122–133. [CrossRef]

79. Distefano, F.; Epasto, G.; Guglielmino, E.; Amata, A.; Mineo, R. Subsidence of a Partially Porous Titanium Lumbar Cage Produced by Electron Beam Melting Technology. *J. Biomed. Mater. Res. B Appl. Biomater.* **2023**, *111*, 590–598. [CrossRef]

80. Li, Y.; Yang, C.; Zhao, H.; Qu, S.; Li, X.; Li, Y. New Developments of Ti-Based Alloys for Biomedical Applications. *Materials* **2014**, *7*, 1709–1800. [CrossRef]

81. Che, Z.; Sun, Y.; Luo, W.; Zhu, L.; Li, Y.; Zhu, C.; Liu, T.; Huang, L. Bifunctionalized Hydrogels Promote Angiogenesis and Osseointegration at the Interface of Three-Dimensionally Printed Porous Titanium Scaffolds. *Mater. Des.* **2022**, *223*, 111118. [CrossRef]

82. Zhao, H.; Shen, S.; Zhao, L.; Xu, Y.; Li, Y.; Zhuo, N. 3D Printing of Dual-Cell Delivery Titanium Alloy Scaffolds for Improving Osseointegration through Enhancing Angiogenesis and Osteogenesis. *BMC Musculoskelet. Disord.* **2021**, *22*, 734. [CrossRef]

83. Gao, P.; Fan, B.; Yu, X.; Liu, W.; Wu, J.; Shi, L.; Yang, D.; Tan, L.; Wan, P.; Hao, Y.; et al. Biofunctional Magnesium Coated Ti6Al4V Scaffold Enhances Osteogenesis and Angiogenesis in Vitro and in Vivo for Orthopedic Application. *Bioact. Mater.* **2020**, *5*, 680–693. [CrossRef] [PubMed]

84. Xu, X.; Lu, Y.; Li, S.; Guo, S.; He, M.; Luo, K.; Lin, J. Copper-Modified Ti6Al4V Alloy Fabricated by Selective Laser Melting with pro-Angiogenic and Anti-Inflammatory Properties for Potential Guided Bone Regeneration Applications. *Mater. Sci. Eng. C* **2018**, *90*, 198–210. [CrossRef] [PubMed]

85. Lv, J.; Xiu, P.; Tan, J.; Jia, Z.; Cai, H.; Liu, Z. Enhanced Angiogenesis and Osteogenesis in Critical Bone Defects by the Controlled Release of BMP-2 and VEGF: Implantation of Electron Beam Melting-Fabricated Porous Ti6Al4V Scaffolds Incorporating Growth Factor-Doped Fibrin Glue. *Biomed. Mater.* **2015**, *10*, 035013. [CrossRef] [PubMed]

86. Efraim, Y.; Schoen, B.; Zahran, S.; Davidov, T.; Vasilyev, G.; Baruch, L.; Zussman, E.; Machluf, M. 3D Structure and Processing Methods Direct the Biological Attributes of ECM-Based Cardiac Scaffolds. *Sci. Rep.* **2019**, *9*, 5578. [CrossRef] [PubMed]

87. van Bael, S.; Chai, Y.C.; Truscello, S.; Moesen, M.; Kerckhofs, G.; van Oosterwyck, H.; Kruth, J.P.; Schrooten, J. The Effect of Pore Geometry on the in Vitro Biological Behavior of Human Periosteum-Derived Cells Seeded on Selective Laser-Melted Ti6Al4V Bone Scaffolds. *Acta Biomater.* **2012**, *8*, 2824–2834. [CrossRef] [PubMed]

88. Cheng, A.; Humayun, A.; Cohen, D.J.; Boyan, B.D.; Schwartz, Z. Additively Manufactured 3D Porous Ti-6Al-4V Constructs Mimic Trabecular Bone Structure and Regulate Osteoblast Proliferation, Differentiation and Local Factor Production in a Porosity and Surface Roughness Dependent Manner. *Biofabrication* **2014**, *6*, 045007. [CrossRef] [PubMed]

89. Prananingrum, W.; Naito, Y.; Galli, S.; Bae, J.; Sekine, K.; Hamada, K.; Tomotake, Y.; Wennerberg, A.; Jimbo, R.; Ichikawa, T. Bone Ingrowth of Various Porous Titanium Scaffolds Produced by a Moldless and Space Holder Technique: An in Vivo Study in Rabbits. *Biomed. Mater.* **2016**, *11*, 015012. [CrossRef] [PubMed]

90. Li, G.; Wang, L.; Pan, W.; Yang, F.; Jiang, W.; Wu, X.; Kong, X.; Dai, K.; Hao, Y. In Vitro and In Vivo Study of Additive Manufactured Porous Ti6Al4V Scaffolds for Repairing Bone Defects. *Sci. Rep.* **2016**, *6*, 34072. [CrossRef]

91. Taniguchi, N.; Fujibayashi, S.; Takemoto, M.; Sasaki, K.; Otsuki, B.; Nakamura, T.; Matsushita, T.; Kokubo, T.; Matsuda, S. Effect of Pore Size on Bone Ingrowth into Porous Titanium Implants Fabricated by Additive Manufacturing: An in Vivo Experiment. *Mater. Sci. Eng. C* **2016**, *59*, 690–701. [CrossRef]

92. Kapat, K.; Srivas, P.K.; Rameshbabu, A.P.; Maity, P.P.; Jana, S.; Dutta, J.; Majumdar, P.; Chakrabarti, D.; Dhara, S. Influence of Porosity and Pore-Size Distribution in Ti6Al4 v Foam on Physicomechanical Properties, Osteogenesis, and Quantitative Validation of Bone Ingrowth by Micro-Computed Tomography. *ACS Appl. Mater. Interfaces* **2017**, *9*, 39235–39248. [CrossRef]

93. Ran, Q.; Yang, W.; Hu, Y.; Shen, X.; Yu, Y.; Xiang, Y.; Cai, K. Osteogenesis of 3D Printed Porous Ti6Al4V Implants with Different Pore Sizes. *J. Mech. Behav. Biomed. Mater.* **2018**, *84*, 1–11. [CrossRef]

94. Luan, H.Q.; Wang, L.T.; Ren, W.Y.; Chu, Z.W.; Huang, Y.F.; Lu, C.L.; Fan, Y.B. The Effect of Pore Size and Porosity of Ti6Al4V Scaffolds on MC3T3-E1 Cells and Tissue in Rabbits. *Sci. China Technol. Sci.* **2019**, *62*, 1160–1168. [CrossRef]

95. Ouyang, P.; Dong, H.; He, X.; Cai, X.; Wang, Y.; Li, J.; Li, H.; Jin, Z. Hydromechanical Mechanism behind the Effect of Pore Size of Porous Titanium Scaffolds on Osteoblast Response and Bone Ingrowth. *Mater. Des.* **2019**, *183*, 108151. [CrossRef]

96. Chen, Z.; Yan, X.; Yin, S.; Liu, L.; Liu, X.; Zhao, G.; Ma, W.; Qi, W.; Ren, Z.; Liao, H.; et al. Influence of the Pore Size and Porosity of Selective Laser Melted Ti6Al4V ELI Porous Scaffold on Cell Proliferation, Osteogenesis and Bone Ingrowth. *Mater. Sci. Eng. C* **2020**, *106*, 110289. [CrossRef] [PubMed]

97. Wang, C.; Xu, D.; Lin, L.; Li, S.; Hou, W.; He, Y.; Sheng, L.; Yi, C.; Zhang, X.; Li, H.; et al. Large-Pore-Size Ti6Al4V Scaffolds with Different Pore Structures for Vascularized Bone Regeneration. *Mater. Sci. Eng. C* **2021**, *131*, 112499. [CrossRef] [PubMed]

98. Sidambe, A.T. Biocompatibility of Advanced Manufactured Titanium Implants-A Review. *Materials* **2014**, *7*, 8168–8188. [CrossRef]

99. Zhang, Z.; Jones, D.; Yue, S.; Lee, P.D.; Jones, J.R.; Sutcliffe, C.J.; Jones, E. Hierarchical Tailoring of Strut Architecture to Control Permeability of Additive Manufactured Titanium Implants. *Mater. Sci. Eng. C* **2013**, *33*, 4055–4062. [CrossRef]

100. Chen, C.; Hao, Y.; Bai, X.; Ni, J.; Chung, S.M.; Liu, F.; Lee, I.S. 3D Printed Porous Ti6Al4V Cage: Effects of Additive Angle on Surface Properties and Biocompatibility; Bone Ingrowth in Beagle Tibia Model. *Mater. Des.* **2019**, *175*, 107824. [CrossRef]

101. Li, Z.; Liu, C.; Wang, B.; Wang, C.; Wang, Z.; Yang, F.; Gao, C.; Liu, H.; Qin, Y.; Wang, J. Heat Treatment Effect on the Mechanical Properties, Roughness and Bone Ingrowth Capacity of 3D Printing Porous Titanium Alloy. *RSC Adv.* **2018**, *8*, 12471–12483. [CrossRef]

102. Beese, A.M.; Carroll, B.E. Review of Mechanical Properties of Ti-6Al-4V Made by Laser-Based Additive Manufacturing Using Powder Feedstock. *JOM* **2016**, *68*, 724–734. [CrossRef]

103. Epasto, G.; Palomba, G.; D'Andrea, D.; Guglielmino, E.; di Bella, S.; Traina, F. Ti-6Al-4V ELI Microlattice Structures Manufactured by Electron Beam Melting: Effect of Unit Cell Dimensions and Morphology on Mechanical Behaviour. *Mater. Sci. Eng. A* **2019**, *753*, 31–41. [CrossRef]

104. Osterhoff, G.; Morgan, E.F.; Shefelbine, S.J.; Karim, L.; Mcnamara, L.M.; Augat, P. Bone Mechanical Properties and Changes with Osteoporosis. *Injury* **2016**, *47* (Suppl. 2), S11–S20. [CrossRef]

105. Sharir, A.; Barak, M.M.; Shahar, R. Whole Bone Mechanics and Mechanical Testing. *Vet. J.* **2008**, *177*, 8–17. [CrossRef]

106. Mirzaali, M.J.; Schwiedrzik, J.J.; Thaiwichai, S.; Best, J.P.; Michler, J.; Zysset, P.K.; Wolfram, U. Mechanical Properties of Cortical Bone and Their Relationships with Age, Gender, Composition and Microindentation Properties in the Elderly. *Bone* **2016**, *93*, 196–211. [CrossRef]

107. Hansen, U.; Zioupos, P.; Simpson, R.; Currey, J.D.; Hynd, D. The Effect of Strain Rate on the Mechanical Properties of Human Cortical Bone. *J. Biomech. Eng.* **2008**, *130*, 011011. [CrossRef]

108. Currey, J.D. *Bones: Structure and Mechanics*; Princetion University Press: Princeton, NJ, USA, 2006.

109. Keaveny, T.M.; Morgan, E.F.; Niebur, G.L.; Yeh, O.C. Biomechanics of Trabecular Bone. *Annu. Rev. Biomed. Eng.* **2001**, *3*, 307–333. [CrossRef]

110. Homminga, J.; Mccreadie, B.R.; Ciarelli, T.E.; Weinans, H.; Goldstein, S.A.; Huiskes, R. Cancellous Bone Mechanical Properties From Normals and Patients With Hip Fractures Differ on the Structure Level, Not on the Bone Hard Tissue Level. *Bone* **2002**, *30*, 759–764. [CrossRef]

111. Nune, K.C.; Misra, R.D.K.; Li, S.J.; Hao, Y.L.; Zhang, W. The Functional Response of Bioactive Titania-Modified Three-Dimensional Ti-6Al-4V Mesh Structure toward Providing a Favorable Pathway for Intercellular Communication and Osteoincorporation. *J. Biomed. Mater. Res. A* **2016**, *104*, 2488–2501. [CrossRef]

112. Sing, S.L.; Yeong, W.Y.; Wiria, F.E. Selective Laser Melting of Titanium Alloy with 50 Wt% Tantalum: Microstructure and Mechanical Properties. *J. Alloys Compd.* **2016**, *660*, 461–470. [CrossRef]

113. Hollister, S.J. Scaffold Design and Manufacturing: From Concept to Clinic. *Adv. Mater.* **2009**, *21*, 3330–3342. [CrossRef] [PubMed]

114. Ghouse, S.; Reznikov, N.; Boughton, O.R.; Babu, S.; Ng, K.C.G.; Blunn, G.; Cobb, J.P.; Stevens, M.M.; Jeffers, J.R.T. The Design and in Vivo Testing of a Locally Stiffness-Matched Porous Scaffold. *Appl. Mater. Today* **2019**, *15*, 377–388. [CrossRef] [PubMed]

115. Wieding, J.; Lindner, T.; Bergschmidt, P.; Bader, R. Biomechanical Stability of Novel Mechanically Adapted Open-Porous Titanium Scaffolds in Metatarsal Bone Defects of Sheep. *Biomaterials* **2015**, *46*, 35–47. [CrossRef] [PubMed]

116. Sun, J.; Wang, Q.; Cai, D.; Gu, W.; Ma, Y.; Sun, Y.; Wei, Y.; Yuan, F. A Lattice Topology Optimization of Cervical Interbody Fusion Cage and Finite Element Comparison with ZK60 and Ti-6Al-4V Cages. *BMC Musculoskelet. Disord.* **2021**, *22*, 390. [CrossRef] [PubMed]

117. Ashby, M.F. The Properties of Foams and Lattices. *Philos. Trans. R. Soc. A Math. Phys. Eng. Sci.* **2006**, *364*, 15–30. [CrossRef] [PubMed]

118. Deshpande, V.S.; Ashby, M.F.; Fleck, N.A. Foam Topology Bending versus Stretching Dominated Architectures. *Acta Mater.* **2001**, *49*, 1035–1040. [CrossRef]

119. Wang, N.; Meenashisundaram, G.K.; Kandilya, D.; Fuh, J.Y.H.; Dheen, S.T.; Kumar, A.S. A Biomechanical Evaluation on Cubic, Octet, and TPMS Gyroid Ti6Al4V Lattice Structures Fabricated by Selective Laser Melting and the Effects of Their Debris on Human Osteoblast-like Cells. *Biomater. Adv.* **2022**, *137*, 212829. [CrossRef]

120. Crupi, V.; Kara, E.; Epasto, G.; Guglielmino, E.; Aykul, H. Static Behavior of Lattice Structures Produced via Direct Metal Laser Sintering Technology. *Mater. Des.* **2017**, *135*, 246–256. [CrossRef]

121. Bai, L.; Xu, Y.; Chen, X.; Xin, L.; Zhang, J.; Li, K.; Sun, Y. Improved Mechanical Properties and Energy Absorption of Ti6Al4V Laser Powder Bed Fusion Lattice Structures Using Curving Lattice Struts. *Mater. Des.* **2021**, *211*, 110140. [CrossRef]

122. Horn, T.J.; Harrysson, O.L.A.; Marcellin-Little, D.J.; West, H.A.; Lascelles, B.D.X.; Aman, R. Flexural Properties of Ti6Al4V Rhombic Dodecahedron Open Cellular Structures Fabricated with Electron Beam Melting. *Addit. Manuf.* **2014**, *1*, 2–11. [CrossRef]

123. Sun, Q.; Sun, J.; Guo, K.; Wang, L. Compressive Mechanical Properties and Energy Absorption Characteristics of SLM Fabricated Ti6Al4V Triply Periodic Minimal Surface Cellular Structures. *Mech. Mater.* **2022**, *166*, 104241. [CrossRef]

124. Sokollu, B.; Gulcan, O.; Konukseven, E.I. Mechanical Properties Comparison of Strut-Based and Triply Periodic Minimal Surface Lattice Structures Produced by Electron Beam Melting. *Addit. Manuf.* **2022**, *60*, 103199. [CrossRef]

125. Naghavi, S.A.; Tamaddon, M.; Marghoub, A.; Wang, K.; Babamiri, B.B.; Hazeli, K.; Xu, W.; Lu, X.; Sun, C.; Wang, L.; et al. Mechanical Characterisation and Numerical Modelling of TPMS-Based Gyroid and Diamond Ti6Al4V Scaffolds for Bone Implants: An Integrated Approach for Translational Consideration. *Bioengineering* **2022**, *9*, 504. [CrossRef] [PubMed]

126. Alabort, E.; Barba, D.; Reed, R.C. Design of Metallic Bone by Additive Manufacturing. *Scr. Mater.* **2019**, *164*, 110–114. [CrossRef]

127. Polley, C.; Radlof, W.; Hauschulz, F.; Benz, C.; Sander, M.; Seitz, H. Morphological and Mechanical Characterisation of Three-Dimensional Gyroid Structures Fabricated by Electron Beam Melting for the Use as a Porous Biomaterial. *J. Mech. Behav. Biomed. Mater.* **2022**, *125*, 104882. [CrossRef]

128. Ataee, A.; Li, Y.; Brandt, M.; Wen, C. Ultrahigh-Strength Titanium Gyroid Scaffolds Manufactured by Selective Laser Melting (SLM) for Bone Implant Applications. *Acta Mater.* **2018**, *158*, 354–368. [CrossRef]

129. Gao, H.; Li, X.; Wang, C.; Ji, P.; Wang, C. Mechanobiologically Optimization of a 3D Titanium-Mesh Implant for Mandibular Large Defect: A Simulated Study. *Mater. Sci. Eng. C* **2019**, *104*, 109934. [CrossRef] [PubMed]

130. Liu, R.; Su, Y.; Yang, W.; Wu, K.; Du, R.; Zhong, Y. A Novel Design Method of Gradient Porous Structure for Stabilized and Lightweight Mandibular Prosthesis. *Bioengineering* **2022**, *9*, 424. [CrossRef]

131. Bittredge, O.; Hassanin, H.; El-Sayed, M.A.; Eldessouky, H.M.; Alsaleh, N.A.; Alrasheedi, N.H.; Essa, K.; Ahmadein, M. Fabrication and Optimisation of Ti-6Al-4V Lattice-Structured Total Shoulder Implants Using Laser Additive Manufacturing. *Materials* **2022**, *15*, 3095. [CrossRef]

132. Fogel, G.; Martin, N.; Lynch, K.; Pelletier, M.H.; Wills, D.; Wang, T.; Walsh, W.R.; Williams, G.M.; Malik, J.; Peng, Y.; et al. Subsidence and Fusion Performance of a 3D-Printed Porous Interbody Cage with Stress-Optimized Body Lattice and Microporous Endplates—A Comprehensive Mechanical and Biological Analysis. *Spine J.* **2022**, *22*, 1028–1037. [CrossRef]

133. Cuzzocrea, F.; Ivone, A.; Jannelli, E.; Fioruzzi, A.; Ferranti, E.; Vanelli, R.; Benazzo, F. PEEK versus Metal Cages in Posterior Lumbar Interbody Fusion: A Clinical and Radiological Comparative Study. *Musculoskelet. Surg.* **2019**, *103*, 237–241. [CrossRef]

134. Nemoto, O.; Asazuma, T.; Yato, Y.; Imabayashi, H.; Yasuoka, H.; Fujikawa, A. Comparison of Fusion Rates Following Transforaminal Lumbar Interbody Fusion Using Polyetheretherketone Cages or Titanium Cages with Transpedicular Instrumentation. *Eur. Spine J.* **2014**, *23*, 2150–2155. [CrossRef] [PubMed]

135. Tanida, S.; Fujibayashi, S.; Otsuki, B.; Masamoto, K.; Takahashi, Y.; Nakayama, T.; Matsuda, S. Vertebral Endplate Cyst as a Predictor of Nonunion after Lumbar Interbody Fusion: Comparison of Titanium And Polyetheretherketone Cages. *Spine* **2016**, *41*, E1216–E1222. [CrossRef] [PubMed]
136. Gok, M.G. Creation and Finite-Element Analysis of Multi-Lattice Structure Design in Hip Stem Implant to Reduce the Stress-Shielding Effect. *Proc. Inst. Mech. Eng. Part L J. Mater. Des. Appl.* **2022**, *236*, 429–439. [CrossRef]